

A deep i-selected multi-waveband galaxy catalogue in the COSMOS field†

A. Gabasch^{1,2,3*}, Y. Goranova^{1,2,5}, U. Hopp^{1,2}, S. Noll^{1,4} and M. Pannella¹

¹Max-Planck-Institut für extraterrestrische Physik, Giessenbachstr., Postfach 1312, D-85741 Garching, Germany

²Universitätssternwarte München, Scheinerstr. 1, D-81673 München, Germany

³European Southern Observatory, 85748 Garching, Germany

⁴Observatoire Astronomique Marseille Provence, Laboratoire d’Astrophysique de Marseille, Traverse du Siphon, 13376 Marseille Cedex 12, France

⁵Leiden Observatory, P.O. Box 9513, NL-2300 RA Leiden, The Netherlands

Accepted Received; in original form

ABSTRACT

In this paper we present a deep and homogeneous i-band selected multi-waveband catalogue in the COSMOS field covering an area of about 0.7° . Our catalogue with a formal 50% completeness limit for point sources of $i \sim 26.7$ comprises about 290 000 galaxies with information in 8 passbands. We combine publicly available u, B, V, r, i, z, and K data with proprietary imaging in H band. We discuss in detail the observations, the data reduction, and the photometric properties of the H-band data. We estimate photometric redshifts for all the galaxies in the catalogue. A comparison with 162 spectroscopic redshifts in the redshift range $0 \lesssim z \lesssim 3$ shows that the achieved accuracy of the photometric redshifts is $\Delta z / (z_{\text{spec}} + 1) \lesssim 0.035$ with only $\sim 2\%$ outliers. We derive absolute UV magnitudes and investigate the evolution of the luminosity function evaluated in the restframe UV (1500 Å). There is a good agreement between the LFs derived here and the LFs derived in the FORS Deep Field. We see a similar brightening of M^* and a decrease of ϕ^* with redshift. The catalogue including the photometric redshift information is made publicly available.

Key words: galaxies: evolution – galaxies: fundamental parameters – galaxies: luminosity function – galaxies: photometry – galaxies: high-redshift

1 INTRODUCTION

In the last decade our knowledge about the evolution of global galaxy properties over a large redshift range has improved considerably. The 2dF Galaxy Redshift Survey (2dFGRS; Colless et al. 2001), the Sloan Digital Sky Survey (SDSS; Stoughton et al. 2002), and the 2MASS survey (Jarrett et al. 2000) have provided very large local galaxy samples with spectroscopic and/or photometric information in various passbands. Thanks to these data sets we are now able to assess very accurate local ($z \sim 0.1$) reference points for many galaxy evolution measurements like the luminosity function, the star formation activity, the spatial clustering of galaxies, the stellar population, the morphology, etc.

In the redshift range between $0.2 \lesssim z \lesssim 1$ pioneer-

ing work has been done in the context of the Canada France Redshift Survey (Lilly et al. 1995), the Autofib survey (Ellis et al. 1996) and in the Canadian Network for Observational Cosmology survey (Yee et al. 1996). They provide accurate distances and absolute luminosities by spectroscopic followup of optically selected galaxies, thus being able to probe basic properties of galaxy evolution. Moreover the K20-survey (Cimatti et al. 2002) as well as the MUNICS survey (Drory et al. 2001a; Feulner et al. 2003) extend the analysis into the near infrared regime (for $0.2 \lesssim z \lesssim 1.5$).

An important step towards probing the galaxy properties also in the high redshift regime around $z \sim 3$ and $z \sim 4$ was the work of Steidel & Hamilton (1993) and Steidel et al. (1996). They used colour selection to discriminate between low and high redshift galaxies (see Giavalisco 2002, for a review). The so-called Lyman-break galaxies (LBGs, mainly starburst galaxies at high redshift) are selected by means of important features in the UV spectrum of star-forming galaxies.

The next milestones in pushing the limiting magnitude for detectable galaxies to fainter and fainter limits

* E-mail: agabasch@eso.org

† Based on observations collected at the Centro Astronómico Hispano Alemán (CAHA), operated jointly by the Max-Planck-Institut für Astronomie, Heidelberg, and the Instituto de Astrofísica de Andalucía (CSIC).

were the space based Hubble Deep Field North (HDFN; Williams et al. 1996a) and Hubble Deep Field South (HDFS; Williams et al. 2000; Casertano et al. 2000) (see Ferguson et al. 2000, for a review). Although of a limited field of view of about $5\Box'$ only, the depth of the HDFs allowed the detection of galaxies up to a redshift of 5 and even beyond.

In the past years the space based HDFs were supplemented by many more multi-band photometric surveys like the NTT SUSI deep Field (NDF; Arnouts et al. 1999a), the Chandra Deep Field South (CDFS; Arnouts et al. 2001a), the William Herschel Deep Field (WHDF; McCracken et al. 2000a; Metcalfe et al. 2001a), the Subaru Deep Field/Survey (SDF; Maihara et al. 2001a; Ouchi et al. 2003), the COMBO-17 survey (Wolf et al. 2003), FIRES (Labbé et al. 2003), the FORS Deep Field (FDF; Heidt et al. 2003), the Great Observatories Origins Deep Survey (GOODS; Giavalisco et al. 2004b), the Ultra Deep Field (UDF and UDF-Parallel ACS fields; Giavalisco et al. 2004a; Bunker et al. 2004; Bouwens et al. 2004), the VIR-MOS deep survey (Le Fèvre et al. 2004), GEMS (Rix et al. 2004), the Keck Deep Fields (Sawicki & Thompson 2005), and the Multiwavelength Survey by Yale-Chile (MUSYC; Gawiser et al. 2006; Quadri et al. 2007).

With the advent of all these deep multi-band photometric surveys the photometric redshift technique (essentially a generalisation of the drop-out technique) can be used to identify high-redshift galaxies. Photometric redshifts are often determined by means of template matching algorithm that applies Bayesian statistics and uses semi-empirical template spectra matched to broad-band photometry (see also Baum 1962; Koo 1985; Brunner et al. 1999; Fernández-Soto et al. 1999; Benítez 2000; Bender et al. 2001; Le Borgne & Rocca-Volmerange 2002; Firth et al. 2006). Redshifts of galaxies that are several magnitudes fainter than typical spectroscopic limits can be determined reliably with an accuracy of $\Delta z/(z_{spec} + 1)$ of 0.02 to 0.1.

In this context the COSMOS survey (Scoville et al. (2007); see also <http://www.astro.caltech.edu/cosmos/> for an overview) combines deep to very-deep multi-waveband information in order to extend the analysis of deep pencil beam surveys to a much bigger volume, thus being able to drastically increase the statistics and detect also very rare objects. For this, the survey covers an area of about $2\Box^\circ$ with imaging by space-based telescopes (Hubble, Spitzer, GALEX, XMM, Chandra) as well as large ground based telescopes (Subaru, VLA, ESO-VLT, UKIRT, NOAO, CFHT, and others).

In this paper we combine publicly available u, B, V, r, i, z, and K COSMOS data with proprietary imaging in the H band to derive a homogeneous multi-waveband catalogue suitable for deriving accurate photometric redshifts. In Section 2 we give an overview of the near-infrared (NIR) data acquisition and we describe our 2-pass data reduction pipeline used to derive optimally (in terms of signal-to-noise for faint sources) stacked images in Section 3. We also present NIR galaxy number counts and compare them with the literature.

In Section 4 we present the deep multi-waveband i-band selected catalogue and discuss its properties, whereas the data reduction of the spectroscopic redshifts is described in

Section 5. In Section 6 we present the photometric redshift catalogue, discuss the accuracy of the latter and show the redshift distribution of the galaxies. In Section 7 we derive the redshift evolution of the restframe UV luminosity function and luminosity density at 1500 Å from our i-selected catalogue before we summarise our findings in Section 8.

We use AB magnitudes and adopt a Λ cosmology throughout the paper with $\Omega_M = 0.3$, $\Omega_\Lambda = 0.7$, and $H_0 = 70 \text{ km s}^{-1} \text{ Mpc}^{-1}$.

2 NIR OBSERVATIONS

2.1 Field layout

Our observing strategy was designed to follow-up the publicly available COSMOS observations with proprietary imaging in H band. The whole area is covered by 25 pointings ($15.4' \times 15.4'$ each) to a depth adequate to the public NIR data. The field layout and nomenclature is shown in Fig.4. The programme was carried out as a joint effort between three large extragalactic survey projects currently being pursued at the Centro Astronómico Hispano Alemán (CAHA), on Calar Alto: ALHAMBRA (Moles et al. 2005), MANOS-wide (Röser et al. 2004; Zatloukal et al. 2007) and MUNICS-Deep (Goranova et al., in prep.). In addition, as a part of the MUNICS-Deep project, in one of the pointings (01c) we have already collected deep Js- and K'-band data.

2.2 Data acquisition

The observations in H, Js and K' bands were carried out using the NIR wide-field imager OMEGA2000¹, operating at the prime focus of the CAHA 3.5m telescope. OMEGA2000 is equipped with a HAWAII-2 HgCdTe 2048x2048 array. The instrument pixel scale is $0.45''$ per pixel, providing a field-of-view of $15.4' \times 15.4'$.

Here we present the H-band observations in 15 pointings (see Fig.4), collected during 11 nights spanned over 3 observing campaigns: December 2004, February 2005, and March/April 2005. Each pointing was observed for a total of at least 3 ksec. The individual exposure times were 3 sec, on-chip co-added to produce single frames of 60 sec each. Except for 05b, at least 50 such frames (depending on the weather conditions) were observed per pointing.

In addition, observations in Js and K' bands in 01c were collected during 7 night in the observing campaigns November 2003 and February 2006. The total exposure time in Js-band data was 8.2 ksec with the same individual exposure time scheme as for the H band. The K'-band observations have a total of 7.7 ksec exposure time with individual exposures of 2 sec, co-added internally into single frames of 30 sec each.

All observations were done using dithering pattern consisting of typically 20 positions shifted with respect to one another by $20''$. The consecutive dithering sequences were repeated with the same pattern but with an offset in the origin.

¹ <http://w3.caha.es/CAHA/Instruments/O2000/index2.html>

Table 1. The 15 COSMOS patches. The table gives the filter, the field name, the coordinates (right ascension α and declination δ) for the equinox 2000, the number of frames, and the total exposure time.

filter	field	α (2000)	δ (2000)	frames	exp. time [ksec]
H	01c	10:01:26.00	+02:26:41.0	93	5.58
	01d	09:59:31.24	+02:26:41.0	81	4.86
	02c	10:00:28.61	+02:26:41.0	84	5.04
	02d	09:58:33.85	+02:26:41.0	100	6.00
	03b	09:59:31.23	+02:41:01.0	50	3.00
	03c	10:01:25.99	+02:12:21.1	50	3.00
	03d	09:59:31.25	+02:12:21.1	50	3.00
	04b	09:58:33.84	+02:41:00.9	74	4.44
	04c	10:00:28.60	+02:12:21.0	49	2.94
	04d	09:58:33.86	+02:12:21.0	50	3.00
	05a	10:01:25.98	+01:58:01.1	49	2.94
	05b	09:59:31.26	+01:58:01.1	24	1.44
	06a	10:00:28.62	+01:58:01.0	70	4.20
	07a	10:01:25.98	+01:43:41.1	61	3.66
	08a	10:00:28.63	+01:43:41.1	48	2.88
Js	01c	10:01:26.00	+02:26:41.0	136	8.16
K'	01c	10:01:26.00	+02:26:41.0	258	7.74

The observing log presenting filters, pointings nomenclature, coordinates, number of frames, and the total exposure time per pointing are listed in Table 1.

3 NIR IMAGING DATA REDUCTION

In this section we present the NIR data reduction in the Js, H, and K' bands. We develop and describe a 2-pass reduction pipeline optimised for reducing and stacking images of different quality to get an optimal signal-to-noise ratio for faint (sky dominated) pointlike objects. We extract Js, H, and K' selected catalogues and show the accuracy of our photometric calibration. Based on these catalogues we compare the number counts in the three NIR filters with number counts taken from the literature.

3.1 Basic reduction

For the basic reduction we use our own reduction pipeline (see Goranova et al., in prep. for a detailed description) based on the IRAF² external package XDIMSUM³. We use a 2-pass reduction implementing object-masking for both flat-field and sky determination. The two passes are as follows:

- First pass:
 - a) Constructing the 1st science-flat,
 - b) Subtracting the sky,
 - c) Masking bad pixels and bad regions,

- d) Rejecting cosmic rays,
- e) Aligning the images, and
- f) Stacking the images

- Second pass:

- g) Constructing the object mask from the stacked image
- h) Masking all objects in the raw frames using the object-mask, repeating pass 1 (step a and b) with masked objects and proceed as in the 1st pass for step c, d, e, and f until final stacking.

The reasons for using this 2-pass reduction pipeline are the following: Due to severe problems with our dome and twilight sky flats (see Goranova et al. in prep.), we derive the flat-fields from the science frames themselves. In such a case, however, it is mandatory to ensure that the final flat-field is free of object residuals. Due to the very high noise level in the raw NIR data, this is possible only if all objects (both the bright and the faint ones) are masked out properly before deriving the flat-field, which we could not achieve with any other objects rejection algorithms ($\kappa - \sigma$ clipping, min-max rejection, etc.) we have applied. An example is presented in Fig. 1, where we show the ratio between the first pass (averaging after min-max rejection) and second pass (averaging after min-max rejection and object masking) flat-fields. The black regions clearly show the object residuals in the flat-field used for the first pass. Although the relative systematic error is in the order of only 0.1%, it makes a significant effect in the final stacked image. The reason for this is the very high sky level of the NIR images. In our case the sky level N of a stacked image is at least in the order of 9 million photons. This implies, that the Poissonian error (\sqrt{N}) is about 3000 photons. If we now introduce a systematic error of 0.1%, we end up with an error of 9000 photons. It is therefore clear that we introduce a systematic error of about 3σ . For faint objects, which are detected on the level of a few σ of the sky background, the systematic offset is in the same order as their total flux. In other words, if we introduce a systematic flat-field error of 0.1%, the introduced systematic error is on the same level as the statistical Poissonian error for a sky level of 1 million photons.

Another problem of NIR data reduction is the short-scale time variability of the sky. We subtract the sky using the so-called 'running' sky technique, i.e we determine the sky for each frame individually. For this we take a series of usually 5 frames grouped in time before and after (but excluding) the frame we are subtracting the sky from and we average those using min-max rejection and object masking. This works very well as the sky-illumination does not change much within this short time.

The variability of the sky on the other hand may change the overall shape of the flat-field (derived before sky subtraction). In order to avoid correcting this additive illumination by the multiplicative flat-field, we use the following approach. First we derive flat-fields for each night by averaging all frames from that night using min-max rejection and object masking. Then we average the normalised flat-fields from all nights in order to derive a master flat-field. This master flat-field should be the best approximation to the real shape of the overall sky-flat. Then we fit a 4th-order Chebyshev polynomial to the master flat-field in order to get the shape of the master flat-field and eliminate the pixel-to-

² "IRAF is distributed by the National Optical Astronomy Observatories, which are operated by the Association of Universities for Research in Astronomy, Inc., under cooperative agreement with the National Science Foundation."

³ Experimental Deep Infrared Mosaicing Software; XDIMSUM is a variant of the DIMSUM package developed by P. Eisenhardt, M. Dickinson, S.A. Stanford, and J. Ward. F. Valdes (IRAF group); see also Stanford et al. (1995).

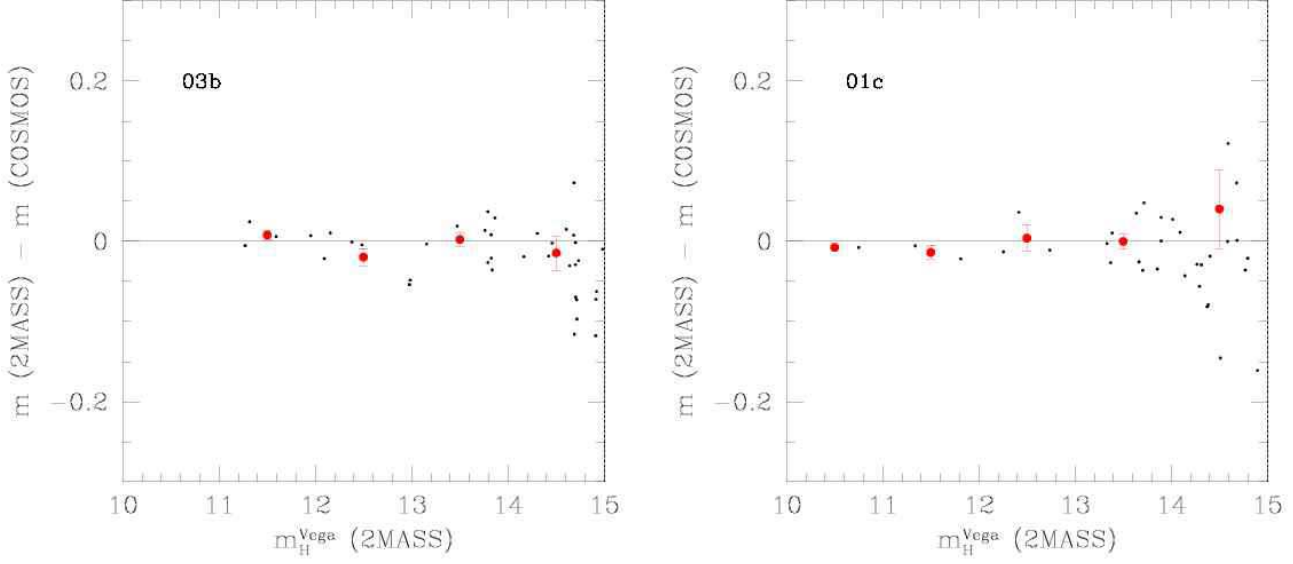


Figure 3. H-band magnitude differences (black dots) between our COSMOS catalogue and 2MASS in 2 fields (03b and 01c). The red symbols show the average in the different magnitude bins. Please note that for these plots we used Vega magnitudes and not AB, in order to avoid adding any systematics by transforming the 2MASS magnitudes to AB system. The error in the zeropoint determination can be found in Table 2.

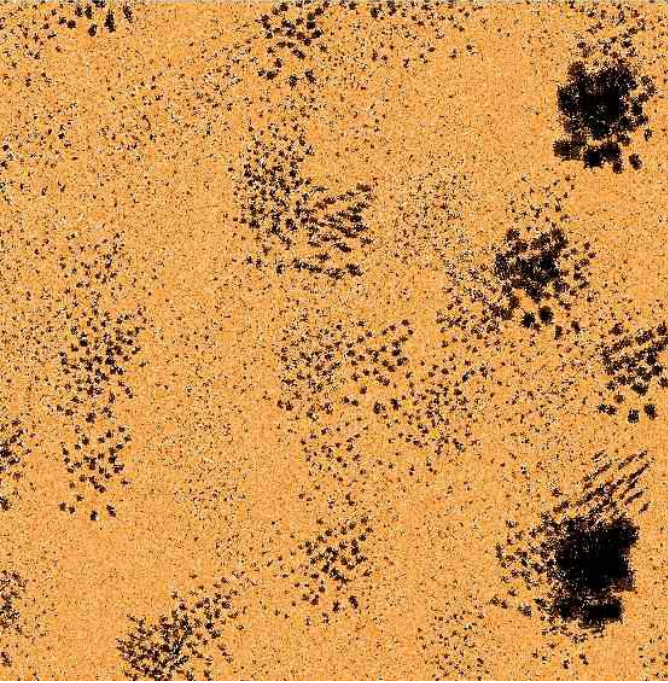


Figure 1. Ratio of first and second pass flat-field: The first pass flat-field has been divided by the second pass flat-field. Dark regions (in the order of 0.1%) represent object residuals in the flat-field after the first pass. See text for details.

pixel variations. Finally, we bend every single flat-field to the shape of the Chebyshev flat-field. The corrections applied to the single flat-fields are in the order of 1–2% (peak to peak).

Table 2. Field characteristics. The first column gives the filter band, the second the field nomenclature as used in Fig. 4. In the third column, the number of detected object is reported (see text for details). The 50% completeness limit follows in the fourth column, the FWHM seeing value in the fifth, and the error of the photometric zero point in the last column.

filter	field	objects	50% CL. [mag]	seeing [$''$]	zeropoint error [mag]
H	01c	2744	21.76	1.13	0.006
	01d	4013	22.38	0.82	0.005
	02c	3483	22.24	0.92	0.007
	02d	3364	22.40	0.98	0.008
	03b	2996	21.82	1.14	0.006
	03c	2020	21.27	1.41	0.007
	03d	2765	21.87	1.24	0.007
	04b	2846	22.25	1.00	0.006
	04c	2567	21.68	1.09	0.006
	04d	2348	21.52	1.39	0.008
Js	05a	1815	21.16	1.07	0.008
	05b	1102	20.60	1.56	0.006
	06a	2981	22.16	0.83	0.008
	07a	1940	21.52	0.80	0.007
	08a	2618	21.83	0.94	0.019
	01c	4005	22.67	0.91	0.009
	01c	3174	21.76	1.05	0.009
	01c	3174	21.76	1.05	0.009

Since our final goal is the combination of our H-band data with public data to construct a multi-wavelength catalogue, we want to astrometrically align our H-band images to the publicly available images in the COSMOS field (Scoville et al. 2007). Moreover, as we intend to use the same procedure as in the FDF in constructing the catalogue (Heidt et al. 2003), i.e. using SExtractor in the double im-

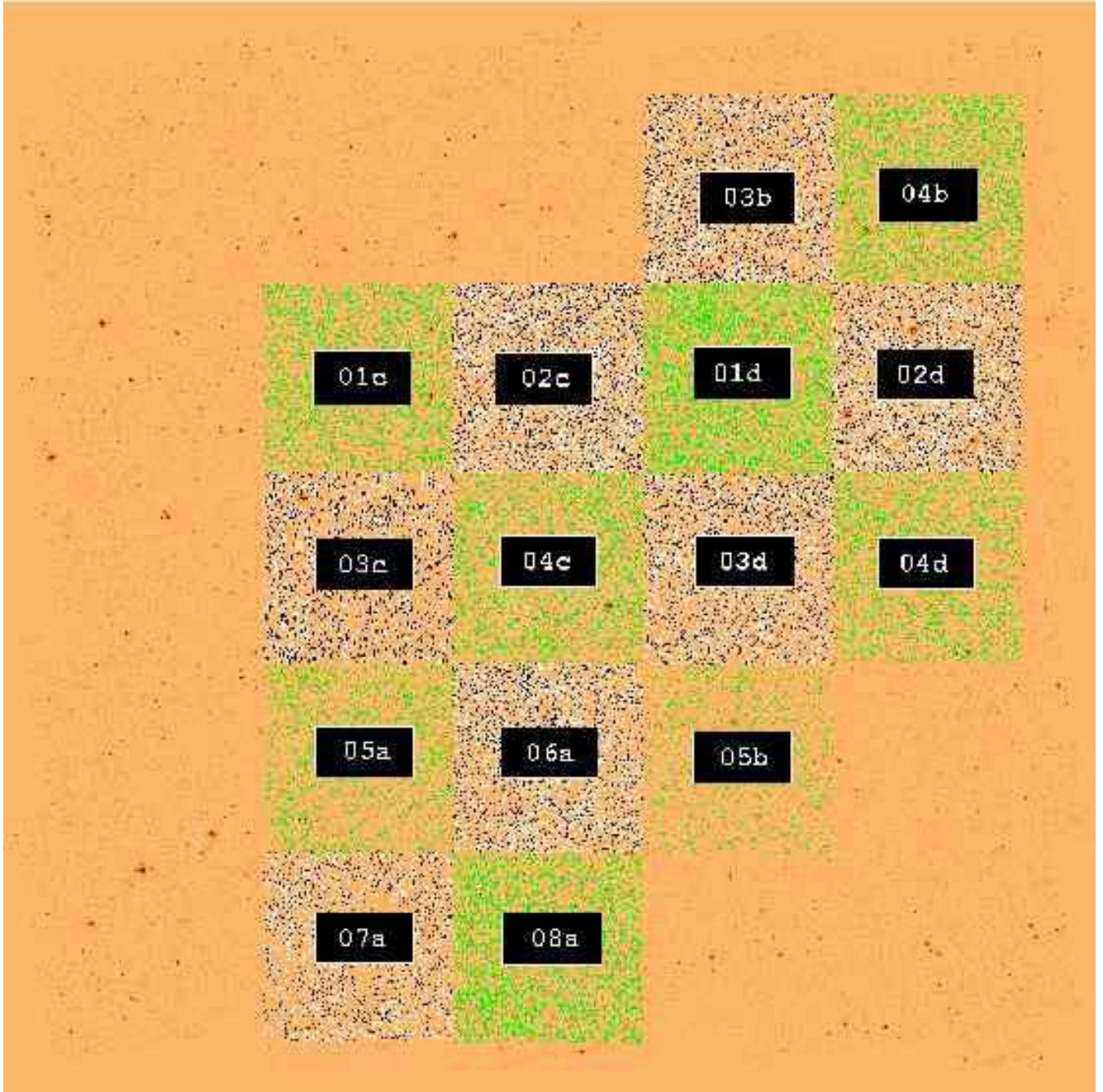


Figure 4. Field nomenclature of the 15 NIR patches together with an excerpt of the H-band detected catalogues (green, black and white for clarity) on top of the HST COSMOS image. Each catalogue covers an area of $205.44''$.

age mode, the data sets in the different passbands must also be aligned by pixel. On the other hand, we do not want to shift the NIR images twice. This would smooth the images and destroy the signal of very faint objects. As it is also very challenging to shift single NIR images on top of deep optical images (where many bright starlike objects are e.g. saturated), we use the following approach:

First we compute the astrometric transformation between our stacked NIR image and the reference optical frame (Subaru *z*-band). This allows us to rely on hundreds of objects when computing the astrometric solution instead of only a

few tenths of objects visible in a single NIR image. Knowing the relative shifts of the single images to the stacked XDIMSUM image and the full astrometric solution of the latter (with respect to the Subaru *z*-band), we are able to calculate the astrometric solution also for each single, *unshifted* pre-reduced image. Restarting from these images, we do the alignment, the distortion correction, the regridding and the stacking of the individual images (with optimal signal-to-noise ratio, see below) in *one* step.

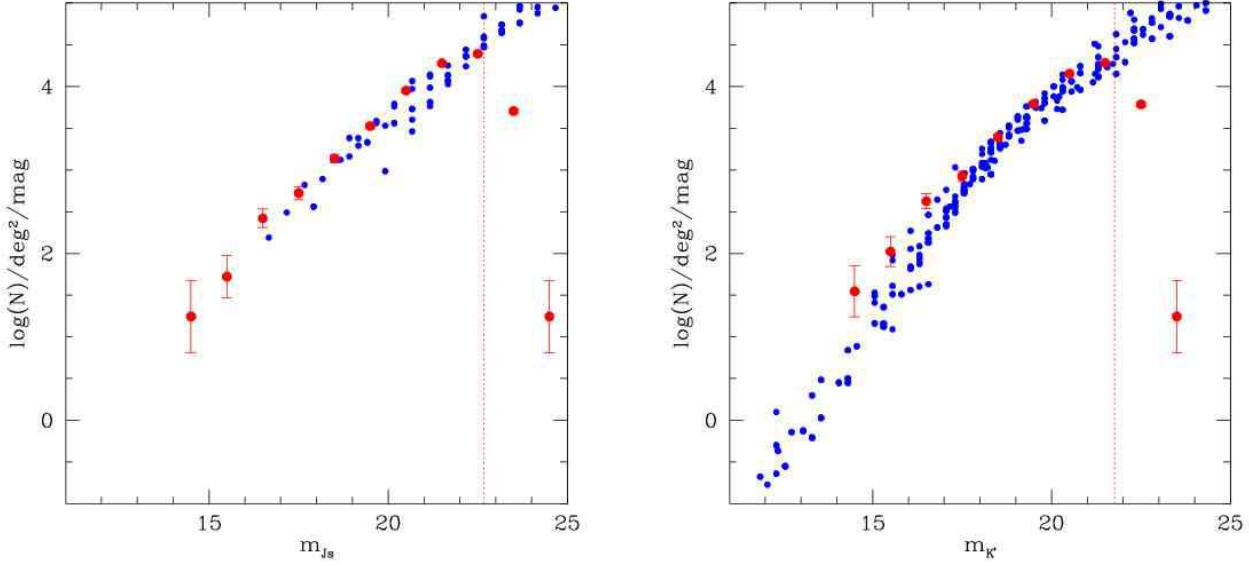


Figure 6. Left panel: Js-band galaxy number counts of patch 01c (red dots, not corrected for incompleteness) as compared to the literature (blue dots). The vertical dotted line indicates the 50% completeness limit. The literature number counts are taken from Saracco et al. (1999, 2001); Maihara et al. (2001b); Teplitz et al. (1999). Right panel: K'-band galaxy number counts of patch 01c (red dots, not corrected for incompleteness) as compared to the literature (blue dots). The vertical dotted line indicates the 50% completeness limit. The literature number counts are taken from Gardner et al. (1993); Soifer et al. (1994); Djorgovski et al. (1995); Glazebrook et al. (1995); McLeod et al. (1995); Gardner et al. (1996); Huang et al. (1997); Moustakas et al. (1997); Saracco et al. (1997); Bershadsky et al. (1998); Szokoly et al. (1998); McCracken et al. (2000b); Väisänen et al. (2000); Drory et al. (2001b); Huang et al. (2001); Kümmel & Wagner (2001); Maihara et al. (2001b); Martini (2001b); Saracco et al. (2001); Cristóbal-Hornillos et al. (2003); Minowa et al. (2005). The error bars show the 1σ Poissonian errors.

3.2 Image stacking with optimal S/N for point sources

As the single exposures were not taken under the same observing conditions, the sky levels, the seeing, and the zero-points can substantially differ from frame to frame. On the other hand this gives one the possibility to stack the single images with weighting factors in order to achieve a final combined frame with optimal signal-to-noise ratio (S/N) for point sources.

We calculated a weight α to be applied to an individual image following the general *Ansatz* for two images (denoted by index 1 and index 2):

$$\begin{aligned} S_{tot} &= S_1 + \alpha_2 S_2 \\ N_{tot} &= \sqrt{N_1^2 + (\alpha_2 N_2)^2} \end{aligned} \quad (1)$$

where S_{tot} and N_{tot} is the signal and the noise of the combined image. This transforms to:

$$\frac{S_{tot}}{N_{tot}} = \frac{f_1 + \alpha_2 f_2}{\sqrt{(f_1 + h_1 \sigma_1^2 \pi) + \alpha_2^2 (f_2 + h_2 \sigma_2^2 \pi)}} \quad (2)$$

where f_1 and f_2 are the fluxes of an object without sky (signal), h_1 and h_2 are the sky values and σ_1 and σ_2 correspond to the seeing in the two frames. α_2 is the weighting factor to be applied to frame 2. It is than straight forward to compute the value of α_2 for which S_{tot}/N_{tot} is maximised:

$$\frac{\partial \frac{S_{tot}}{N_{tot}}}{\partial \alpha_2} \stackrel{!}{=} 0 \Rightarrow \alpha_2 = \frac{f_2(f_1 + h_1 \sigma_1^2 \pi)}{f_1(f_2 + h_2 \sigma_2^2 \pi)} \quad (3)$$

For bright objects which are not dominated by the sky noise ($f \gg h$) Equation (3) approaches the limit

$$\alpha_2 = 1, \quad (4)$$

whereas for faint, sky dominated objects ($f \ll h$) Equation (3) transforms into

$$\alpha_2 = \frac{f_2 \cdot (h_1 \sigma_1^2)}{f_1 \cdot (h_2 \sigma_2^2)} \quad (5)$$

As the overwhelming majority of the objects are very faint point sources and therefore dominated by the sky noise, Equation (5) is used to derive the weighting-parameter α .

To reduce errors when determining the weighting-parameter α , the fluxes $f_{1/2}$ are derived from a bright not saturated star, the sky levels $h_{1/2}$ correspond to the mode⁴ of the image and the seeings $\sigma_{1/2}$ have been calculated from the median seeing of a few stars.

The weighting factor for the 1st frame (randomly chosen) was set to unity. The factors for all other ($N - 1$) images were then derived following Equation (5) relative to this image. The final stacked frame I_{sum} can then be calculated according to:

$$I_{sum} = \sum_{i=1}^N \alpha_i B_i \tilde{I}_i \cdot \frac{\sum_{i=1}^N \alpha_i f_i}{\sum_{i=1}^N \alpha_i f_i B_i} \quad (6)$$

⁴ most frequent value in the pixel histogram of the image



Figure 2. Different steps of the reduction pipeline: A single raw H-band image (upper panel), the same image after pre-reduction (middle panel), and a stacked image after the two-pass data reduction and stacking with optimal S/N ratio (lower panel).

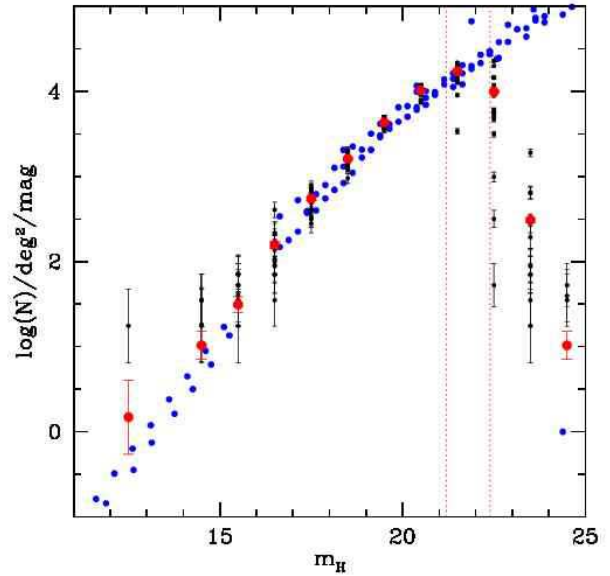


Figure 5. Galaxy number counts in the H-band (not corrected for incompleteness) as compared to the literature (blue dots). The black dots represent the number counts of the single patches, whereas the red dots show the average number counts of all fields. The vertical dotted lines indicate the 50% completeness limits of the shallowest (05a) and the deepest (02d) patches. The literature number counts are taken from Yan et al. (1998); Teplitz et al. (1998); Thompson et al. (1999); Martini (2001a); Chen et al. (2002); Moy et al. (2003); Firth et al. (2006); Metcalfe et al. (2006). The error bars show the 1σ Poissonian errors.

where the index i denotes a single image. α_i is the weighting factor according to Equation (5); \tilde{I}_i is the sky-subtracted single image; B_i is the bad pixel mask⁵ and f_i is the flux derived from the bright star (used to derive α_i ; see also Equation 2).

Finally, we did the image alignment, the distortion correction, the regridding and the stacking of the individual images with optimal S/N in one step by using standard IRAF routines as well as SWarp (Bertin, E. 2003). The regridding has been done to the native pixel scale of the Subaru telescope ($0.2''$ per pixel). Please note that we do not interpolate any bad pixel or bad region in the single images, but set them to zero during the stacking procedure. Missing flux in bad regions is taken into account by using Equation (6). Since a different number of dithered frames contributed to each pixel in the co-added images (producing a position-dependent noise pattern) a combined weight map for each frame was constructed. The latter was used during source detection and photometry procedure to properly account for the position-dependent noise level.

In Fig. 2 we illustrate different steps of our reduction pipeline: a single raw H-band image, the same image after pre-reduction, and a stacked image after the two-pass data reduction and stacking with optimal S/N ratio. There are

⁵ zero for a bad pixel, unity otherwise

practically no haloes around very bright objects, e.g. due to object residuals in the flat-field or sky subtraction problems / residuals.

3.3 Photometric calibration

The absolute photometric calibration is based on the 2MASS (Jarrett et al. 2000) catalogue. First we cross-correlate the objects in all our reduced patches with sources in the 2MASS catalogue. We exclude all objects with possible problems in either one of the catalogues relying on the quality flags of 2MASS and SExtractor quality flags (only objects with a flag of ≤ 3 are considered). An error weighted fit between these objects (20 to 45, depending on the patch) then determines the zeropoint as well as its error. In Fig. 3 we show typical magnitude differences between our COSMOS catalogue and 2MASS. Please note that for these plots we used Vega magnitudes and not the AB magnitude systems (we did not want to add any systematic by changing the 2MASS magnitude system). The accuracy of the zeropoint in the different fields is in the order of 0.01 magnitudes (derived from the error weighted fit between the COSMOS and 2MASS objects; see above) and can be found in Table 2.

3.4 NIR catalogues

Based on the stacked images we derived 15 H-band selected catalogues (see Fig. 4) as well as 1 J-band and 1 K-band selected catalogue (in field 01c, only). For this purpose we run SExtractor (Bertin & Arnouts 1996) with the detection threshold $t = 2$ (minimum signal-to-noise ratio of a pixel to be regarded as a detection) and $n = 3$ (number of contiguous pixels exceeding this threshold). Depending on the depth⁶ of the different patches, we detect between 2000 and 4000 objects (excluding patch 05b where we have only half of the minimum exposure time we wanted to achieve). The false detection rate are in the order of one percent or less (detected on the inverted image). Only around extremely bright and saturated objects (three in patch 02d and one in patch 03c) the false detection rate increases. As the regions around these four objects are not taken into account, we get an overall false detection rate in the order of 1 percent.

Because the depth of the patches decreases towards the borders, we limited our analysis to the inner field. The signal-to-noise ratio in this ‘deep’ region is at least 90% of the best S/N in every patch. This prevents a possible bias of the photometric redshifts due to a not completely homogeneous data set. The single patches, each covering an area of 205.44'' together with the field nomenclature are shown in Fig. 4. In total we detected about 40 000 H-selected objects over an area of about 0.85''^2 as well as about 4000 (3000) J (K) selected galaxies over an area of 205.44''^2 .

3.5 NIR number counts

The galaxy number counts can be used to check the calibration of the data set, to detect possible galaxy over or underdensities of a field as well as to determine the approximate

Table 4. COSMOS (FDF) field characteristics for a SExtractor detection threshold of $t = 2.5$ ($t = 1.7$) and $n = 3$ ($n = 3$) contiguous pixels.

Filter	50 % CL. COSMOS	50 % CL. FDF	seeing [$''$]
u_{CFHT}	25.6	26.5 (U)	0.90
B_{Subaru}	27.7	27.6 (B)	0.95
V_{Subaru}	26.5	26.9 (g)	1.30
r_{Subaru}	26.8	26.9 (R)	1.05
i_{Subaru}	26.7	26.8 (I)	0.95
z_{Subaru}	25.1	25.8 (z)	1.15
Ks_{KPNO}	21.2	22.6 (Ks)	1.28

depth of the data. We did not put much effort in star-galaxy separation at the faint end (as we did for the i-selected catalogue, see Sect. 4), where the galaxies dominate the counts. At the bright end, where SExtractor is able to disentangle a stellar and a galaxy profile, we used the star-galaxy classifier to eliminate obvious stellar objects. We present in Fig. 5 the H-band number counts of all patches and in Fig. 6 the Js and K’ band number counts of patch 01c. Although the single patches show a scatter in the H-band number counts at the very bright end, there is a good to very good agreement between the literature number counts and our mean number counts (red dots) up to the 50 % completeness limit for point sources (Snigula et al. 2002). Comparing the Js and K’ band number counts with data taken from the literature (Fig. 6) also shows a relatively good agreement, although patch 01c seems to be overdense with respect to most of the literature values. This is also true for the H-band number counts in 01c if compared to the other patches or to the literature, indicating an overdensity in this specific patch. Nevertheless, our results are compatible within the error bars at a 1σ level.

Please note that the 50 % completeness levels for point sources (vertical red lines in Fig. 5 and Fig. 6) coincide very nicely with the faint-end region where the number counts start to drop. The values of the NIR galaxy number counts can be found in Table 3.

4 THE I-SELECTED CATALOGUES

Based on the publicly available optical and NIR data of the COSMOS field⁷ we build a Subaru i-band detected galaxy catalogue in 12 of our 15 patches. Because of the relatively bad H-band seeing ($> 1.3''$), we exclude the patches 03c, 04d as well as 05b. We decided to use the ground based i-band for source detection mainly for two reasons: First, at the time when we started the photometric redshift determinations the HST coverage of our reduced H-band patches was not yet completed. Second, including space based data with their superb PSF would need a different technique (with HST images in various wavebands) to optimally construct the multi-waveband catalogue (see e.g. Grazian et al. (2006) for the GOODS-MUSIC sample).

We use a very similar approach as for the FDF (Heidt et al.

⁶ as a result of the slightly varying seeing and total exposure times, see Table 2

⁷ The data were taken from:
<http://irsa.ipac.caltech.edu/data/COSMOS/>

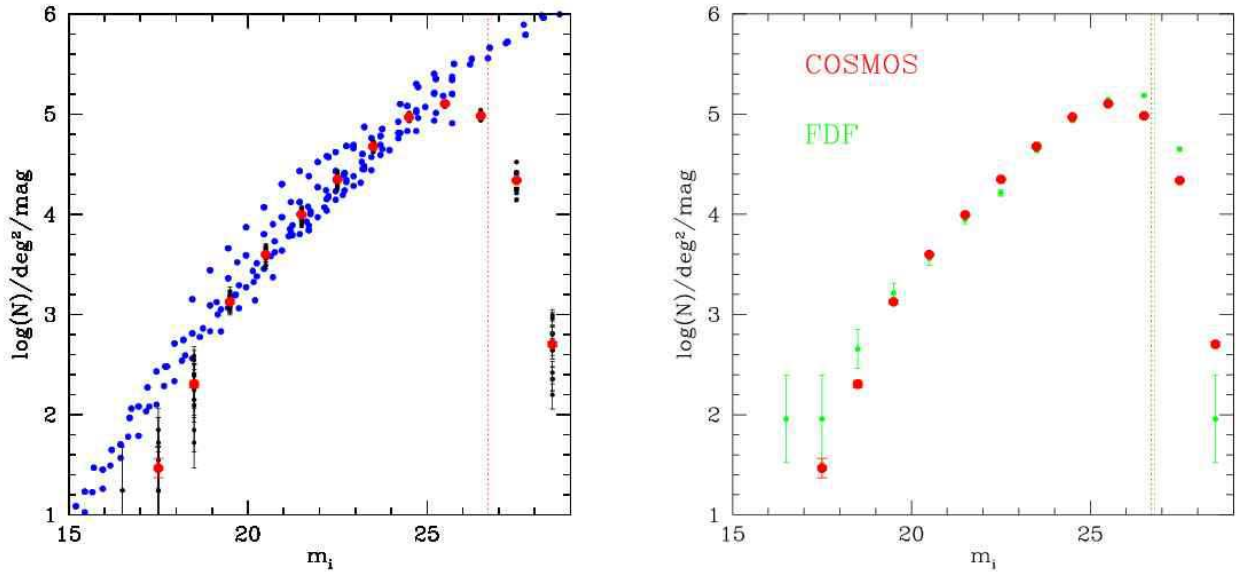


Figure 7. Left panel: Galaxy number counts in the *i*-band (not corrected for incompleteness) as compared to the literature. The black dots represent the number counts of the single COSMOS patches, whereas the red dots show the average number counts of all fields. The vertical dotted line indicates the 50% completeness limit. The literature number counts are taken from Hall & Mackay (1984); Tyson (1988); Lilly et al. (1991); Casertano et al. (1995); Driver et al. (1995); Williams et al. (1996b); Huang et al. (1998); Postman et al. (1998); Arnouts et al. (1999b); Metcalfe et al. (2001b); Arnouts et al. (2001b); Yasuda et al. (2001); Capak et al. (2004). Right panel: Galaxy number counts in the *i*-band (not corrected for incompleteness) as compared to the FDF. The red dots show the average number counts of all COSMOS fields, whereas the green dots show the number counts as derived from the deep part of the FDF. The vertical dotted lines indicate the 50% completeness limits of COSMOS and FDF. The error bars show the 1σ Poissonian errors.

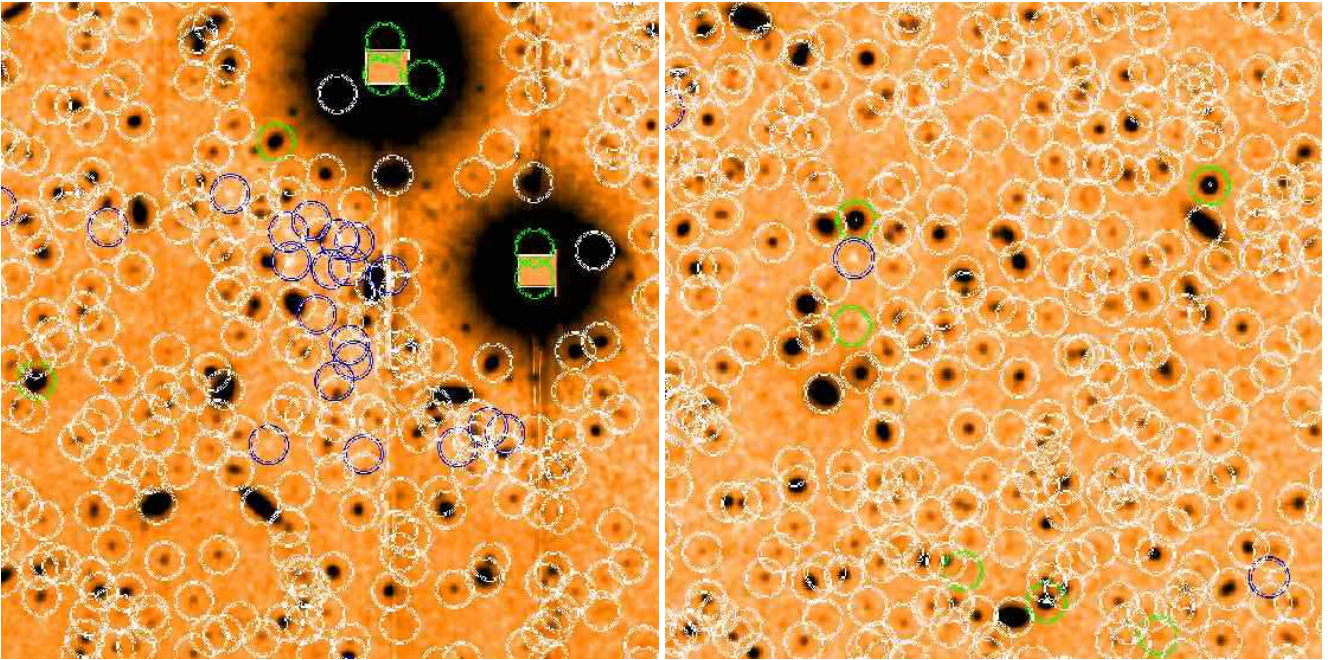


Figure 8. $1.5' \times 1.5'$ Subaru *i*-band image. White circles mark the detected objects from the final catalogue, green circles mark objects eliminated from the final catalogues (saturated or corrupted magnitude, see text for details), whereas the blue circles mark false detections as detected on the negative image. It illustrates the fact, that there are many more detections in the negative image around bright objects (left panel) than in other areas of the image (right panel).

Table 3. Galaxy number counts not corrected for incompleteness from COSMOS in the i (12 patches), J_s (1 patch), H (15 patches), and K' (1 patch) bands. $\log N$ and $\sigma_{\log N}$ are given, where N is in units of $\text{mag}^{-1}\text{deg}^{-2}$.

m	i $\log N$	$\sigma_{\log N}$	J_s $\log N$	$\sigma_{\log N}$	H $\log N$	$\sigma_{\log N}$	K' $\log N$	$\sigma_{\log N}$
14.5			1.244	0.434	1.015	0.164	1.545	0.307
15.5			1.721	0.250	1.492	0.094	2.022	0.177
16.5	0.465	0.307	2.420	0.112	2.195	0.042	2.624	0.088
17.5	1.465	0.097	2.721	0.079	2.738	0.022	2.925	0.062
18.5	2.304	0.036	3.136	0.049	3.206	0.013	3.393	0.036
19.5	3.127	0.014	3.525	0.031	3.631	0.008	3.790	0.023
20.5	3.598	0.008	3.949	0.019	4.010	0.005	4.152	0.015
21.5	3.996	0.005	4.277	0.013	4.236	0.004	4.283	0.013
22.5	4.350	0.003	4.390	0.011	3.995	0.005	3.784	0.023
23.5	4.677	0.002	3.705	0.025	2.486	0.030	1.244	0.434
24.5	4.970	0.001	1.244	0.434	1.015	0.164		
25.5	5.103	0.001			0.170	0.434		
26.5	4.983	0.001						
27.5	4.338	0.003						
28.5	2.702	0.023						
29.5	1.278	0.120						

2003) in constructing a multi-waveband catalogue in the COSMOS field. First we align by pixel all available filters (UCFHT, B_{Subaru}, V_{Subaru}, r_{Subaru}, i_{Subaru}, z_{Subaru}, K_{SKPNO}, afterwards referred to as u, B, V, r, i, z, and K) to our H-band patches and derive i-selected catalogues. Please note that we had to compute a new astrometric solution for the public K band, as the solution given in the images was not sufficiently accurate. The program SCAMP (Bertin 2006) was applied for this procedure. Then we convolved all images to the same seeing of 1.3'' and ran SExtractor in the double image mode with the detection threshold of $t = 2.5$ and $n = 3$ contiguous pixels (we detect on the original i-band image with a seeing of 0.95''). The 50 % completeness limits as well as the seeing of the different bands are listed in Table 4. The Table also compares the depth of the different bands with the depth in the FDF. Beside the u, z, and K bands, the COSMOS data set is roughly as deep as the FDF. In the u-band, z-band as well as in the K band the FDF is about 1 magnitude deeper.

In the FDF we did the source detection with $n = 3$ contiguous pixels and a threshold of $t = 1.7$. This results in only a few false detections (less than 1 percent). For the COSMOS data set we could not use the same detection threshold as this would result in too many false detections (measured on the negative image). We use a threshold of $t = 2.5$ in order to have false detections only at the 1 to 2 percent level. Depending on the patch, the false detections as measured on the negative image fluctuate between 0.6 percent and 2.6 percent. Nevertheless this is not the real contamination rate, as a substantial fraction of these false objects detected on the negative image are distributed around bright objects. On the other hand the number density on the positive side does *not* increase around these bright objects. Therefore it is most likely, that these false detections are due to a reduction problem triggering false detections only in the negative image. This can be seen in Fig. 8 where we show a region around relative bright objects together with the positive and negative detections. Taking this into account, we conclude

that we have a contamination rate of about 1 percent or less in our catalogues.

In total we detected about 300 000 objects in the 12 patches (3 contiguous pixels and a detection threshold of 2.5). These patches have a seeing of less than 1.3'' (see above) in every band and reside in a region which has at least 90% of the maximum depth of each band. Moreover we exclude all objects (based on the weighting maps and SExtractor flags) with problems in the photometry (e.g. if some pixels of an object are saturated or the magnitude is corrupted) in at least one band in order to get a perfectly clean catalogue suitable to derive photometric redshifts. At this stage our clean i-selected catalogue comprises 293 377 objects. As we work on the individual patches and they slightly overlap, we analyse the objects and found that about 99% are unique entries.

A comparison between the i-band number counts in the COSMOS field and in the literature as well as with the FDF are shown in Fig. 7. There is a good agreement between the literature and COSMOS number counts up to the limiting magnitude. Moreover, the comparison with the FDF number counts shows an excellent agreement down to the faintest bins. Only at the very bright end the FDF number counts are slightly higher (most of the very bright objects are saturated in the COSMOS i-band and thus not taken into account), although not by more than 1σ to 2σ . The values of the galaxy number counts can be found in Table 3.

In order to avoid contamination from stars, we rely on two sources of information: The star-galaxy classifier of the detection software SExtractor, and the goodness of fit of the photometric redshift code. We first exclude all bright ($i < 22.5^m$) starlike objects (SExtractor star galaxy classifier > 0.97). Then we exclude all fainter objects whose best fitting stellar spectral energy distribution (SED) – according to the photometric redshift code – gives a better match to the flux in the different passbands than any galaxy template ($2\chi_{star}^2 < \chi_{galaxy}^2$). These objects are subsequently flagged as stars and removed from our galaxy catalogue. In order

to test the accuracy of our procedure we further inspect by eye (in one patch) on the public ACS data if the objects flagged as stars are extended. It turned out that about half of these objects are extended in the ACS data and only half are point-like. Although this approach (see Gabasch et al. 2004a) of excluding stars works very well in the FDF where the seeing of the detection image is only $0.55''$, it is much less effective in the COSMOS *i* band with a seeing of $0.95''$.

In total 4803 (1.6 %) objects were classified as stars and removed from our sample (see also Fig. 13 for the photometric redshift distribution of all starlike objects excluded from the galaxy catalogue). Please note that most of the bright point-like objects are saturated in one of the bands and already removed in the first cleaning step (see above). Therefore our final *i*-band selected galaxy catalogue comprises 288 574 objects.

5 SPECTROSCOPIC REDSHIFTS

Photometric redshifts need to be calibrated by spectroscopic redshifts for objects covering a wide range of galaxy types and redshifts. Hence, we selected spectroscopic data of the COSMOS field (Scoville et al. 2007) from the ESO archive taken with the VIMOS spectrograph (Le Fèvre et al. 2003) at the ESO VLT in the context of the zCOSMOS project (Lilly et al. 2007). zCOSMOS is a Large ESO Programme with 600 hr of observing time aiming at the characterisation of the distribution and properties of galaxies out to redshifts of $z \sim 3$. The project is divided into two parts. zCOSMOS-bright focuses on relatively bright galaxies with $I_{AB} < 22.5$ at redshifts $0.1 < z < 1.2$. In order to include such galaxies in our spectroscopic control sample we selected the VIMOS mask ‘zCOSMOS_4-4’ with 312 slits centred at $10^{\text{h}}00^{\text{m}}28.20^{\text{s}} +02^{\circ}15'45.0''$. This mask was observed 1.5 h with the red low-resolution LR_red grism ($R \sim 210$), covering a wavelength range from 5500 to 9500 Å. zCOSMOS-deep aims at galaxies with $1.5 < z < 2.5$. For this Lilly et al. (2007) selected targets using the *BzK* criteria of Daddi et al. (2004) and the *UGR* ‘BX’ and ‘BM’ selection of Steidel et al. (2004). We obtained a representative sample of such galaxies, reducing the VIMOS mask ‘zCOSMOS_55_faint’ with 239 slits at $10^{\text{h}}00^{\text{m}}27.67^{\text{s}} +02^{\circ}10'23.0''$, observed 4.5 h with the blue low-resolution LR_blue grism ($R \sim 180$), covering a wavelength range from 3700 to 6700 Å.

The spectra of both VIMOS masks were reduced using VIPGI (Scoddeggio et al. 2005). This software package is designed to reduce the multi-object VIMOS spectra in a quite automatic way. The reduction was performed using essentially standard methods. The jittered sequences of individual exposures (five different positions) allowed to efficiently correct for fringing and to obtain a high-quality sky subtraction. The one-dimensional composite spectra were extracted by means of the S/N-optimised Horne (1986) algorithm. The final spectra are flux calibrated and corrected for atmospheric absorption bands.

Redshifts were derived using the cross-correlation based algorithm described by Noll et al. (2004). In order to obtain the redshift and a rough spectral type, we used a sequence of six empirical templates (see Noll et al. 2004, for more details) essentially differing in their UV-to-optical flux ratio, but also showing different strengths of nebular emission

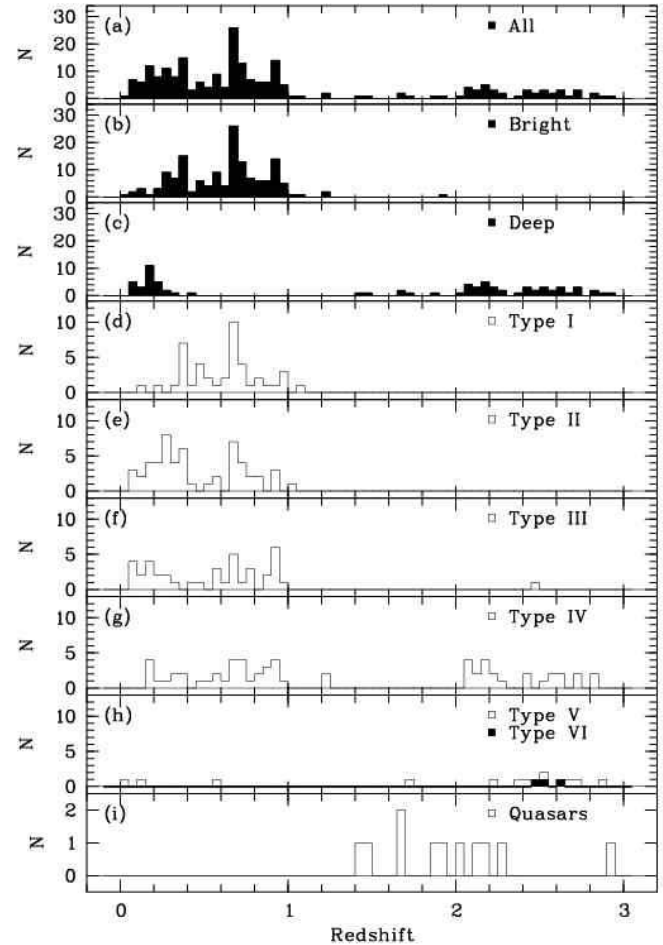


Figure 9. Redshift distribution of the COSMOS spectroscopic sample for (a) all extragalactic objects with trustworthy redshifts, (b) the corresponding objects of the bright-galaxies mask, (c) the corresponding objects of the zCOSMOS-deep mask, (d) – (h) galaxies of different object type, and (i) the quasars. The types range from I = ellipticals (or passively evolving) to V = extreme starbursts (see Noll et al. 2004). In diagram (h) galaxies of type V (white bars) as well as type VI (strong $\text{Ly}\alpha$ emitters, black bars) are plotted. The redshift resolution is $\Delta z = 0.05$.

lines. For the comparison to photometric redshifts we consider galaxies with trustworthy ($> 90\%$ confidence) spectroscopic redshifts only. Due to low S/N (particular at high redshift) and the limited wavelength ranges of the spectra certain redshifts could only be derived for about half of the objects, i.e. 272 of 551 spectra. For the zCOSMOS-deep mask the success rate (33%) is significantly lower than for the bright-galaxy mask (62%). The total sample of 272 objects with trustworthy redshifts includes 49 stars and 12 quasars. Hence, the final sample of galaxies comprises 211 objects. The majority of them (147 or 70%) belongs to the bright-galaxy sample. On the other hand, the subsample of 36 galaxies with redshifts $1.5 < z < 3$ only consists of objects from the zCOSMOS-deep sample. These high-redshift galaxies (quasars excluded) correspond to 45% of the objects identified in the deep sample. Fig. 9 shows the redshift distribution of the full spectroscopic control sample, the ‘zCOSMOS_4-4’ mask, the ‘zCOSMOS_55_faint’ mask,

the different galaxy types defined by Noll et al. (2004, I = ellipticals, V = extreme starbursts, VI = strong Ly α emitters), and the quasars.

After cross-correlating (by visual inspection) the 211 spectroscopic objects with the final i-band selected catalogue in the 12 patches we end up with a final sample of 162 spectroscopic redshifts used to calibrate the photometric redshifts. As the spectroscopic redshift sample was merely used to calibrate the photometric redshift and to measure the accuracy of the photometric redshift code, we decided to use only objects with a unique cross identification. Therefore we excluded all objects where the cross-matching between the photometric and spectroscopic catalogue was not unique, where the objects of the photometric catalogue show saturation in one (or more) image and where the spectroscopic distance determination was not very reliable (e.g. low S/N ratio).

6 PHOTOMETRIC REDSHIFTS

A summary of the photometric redshift technique used to derive the distances to the galaxies can be found in Bender et al. (2001) and Gabasch et al. (2004a). Before deriving the photometric redshifts we checked and fine-tuned the calibration of our photometric zeropoints by means of colour-colour plots of stars. We compared the colours of stars with the colours of stellar templates from the library of Pickles (1998) converted to the COSMOS filter system. In general, corrections to the photometric zeropoints of only a few hundredth of a magnitude were needed to obtain a good match to the stars and best results for the photometric redshifts (if compared to the spectroscopic ones). Only in the u-band and in the K-band, the correction were in the order of a few tenths of a magnitudes. A comparison between the reduced KPNO K-band and our K-band (both convolved to the same seeing of 1.3'') in patch 01c showed, that although the total magnitudes agreed very well, the fixed aperture magnitudes (especially of relatively faint sources) differ systematically by a few tenths of a magnitude. Therefore we decided to correct the KPNO zeropoint by matching the faint sources in the KPNO image with those in our own field (in the fixed aperture used to derive the photometric redshifts). Moreover when calculating the photometric redshifts, we artificially increased the magnitude errors in the K-band by 0.25^m (added in quadrature to the SExtractor errors) to reduce the relative weight of this slightly problematic band. Therefore, we rely mostly on the accurate photometry of the NIR H band.

In order to avoid contamination from close-by objects, we derived object fluxes for a fixed aperture of 2.0'' (1.5 \times seeing) from images which had been convolved to the same point spread function (PSF; 1.3''). A redshift probability function $P(z)$ was then determined for each object by matching the object's fluxes to a set of 29 template spectra redshifted between $z = 0$ and $z = 10$ and covering a wide range of ages and star-formation histories.

In Fig. 10 (left panel) we compare 162 high quality galaxy spectroscopic redshifts with the photometric redshifts. Although there is a good agreement in the redshift range between $z \sim 0.2$ and $z \sim 1.2$, it is clear from Fig. 10, that there is a degeneracy between high redshift ($z \sim 2.5$)

and low redshift ($z \sim 0.2$) objects (10 catastrophic outliers with $\Delta z / (z_{spec} + 1) \gtrsim 0.2$). This degeneracy stems from the relatively red u-band. In Fig. 12 we show the redshift probability function as well as the SED fits to the observed flux of the spectroscopic object 000932543. Although the spectroscopic redshift is $z_{spec} = 0.093$, the best fitting photometric redshift is $z_{phot} = 2.72$. On the other hand, there is also a low redshift peak around $z_{phot} = 0.18$ in the redshift probability function (but with a lower probability). Moreover Fig. 12 also shows that both, the high redshift as well as the low redshift solutions are hard to disentangle as long as no information in the UV is available (as they differ mainly in the UV). Therefore we decided to include in the determination of the photometric redshifts also the GALEX FUV and NUV bands⁸.

As we do not want to convolve all the images to a seeing of 5'' (GALEX PSF), we decided to use another approach to include the UV fluxes in our photometric redshift estimation. Similar to the optical and NIR bands we used a fixed aperture of $\sim 1.5 \times$ PSF, i.e. 7.5''. As there were no obvious features in the colour-colour plots of stars including the UV bands, we could not fine-tune the calibration of the zeropoints by means of colour-colour plots of stars. Therefore we optimised the zeropoints by using the SED fits of our galaxies with very good photometric redshifts (if compared with the spectroscopic ones). Please note that this approach can not derive accurate UV fluxes, but gives only a very rough flux estimation in the two UV bands. Nevertheless, it is now possible to break the degeneracy between the high redshift and low redshift solution. This can be best seen in Fig. 12 where we show one of the catastrophic outliers. Only by including the NUV and FUV fluxes (right panel) we are able to obtain a photometric redshift of $z = 0.08$, hence very close to the spectroscopic redshift of $z_{spec} = 0.093$. This approach drastically reduces the number of our catastrophic photometric redshift outliers (see Fig. 10).

In Fig. 10 (right panel) we compare the final photometric and spectroscopic redshifts of the 162 galaxies. The agreement is very good and we have only 3 catastrophic outliers. The right panel of Fig. 11 shows the distribution of the redshift errors. It is nearly Gaussian and scatters around zero with an rms error of $\Delta z / (z_{spec} + 1) \approx 0.035$. Fig. 11 (left panel) presents the χ^2 distribution of the best fitting templates and photometric redshifts for all the objects. The median value of the reduced χ^2 is 1.5 and demonstrates that the galaxy templates describe the vast majority of galaxies very well. Please note that although the photometric redshift accuracy of a single object does not considerably improve by adding our H-band to the publically available data, the number of catastrophic outliers decreases by nearly a factor of 2. Moreover, the H-band was also very useful to find and address the problems in the public K-band as mentioned before.

The galaxy redshift histogram of all objects in the different patches is shown in Fig. 13. The mean galaxy distribution can be very well described by Equation (7) introduced by Brainerd et al. (1996),

⁸ The data were taken from:
<http://irsa.ipac.caltech.edu/data/COSMOS/>

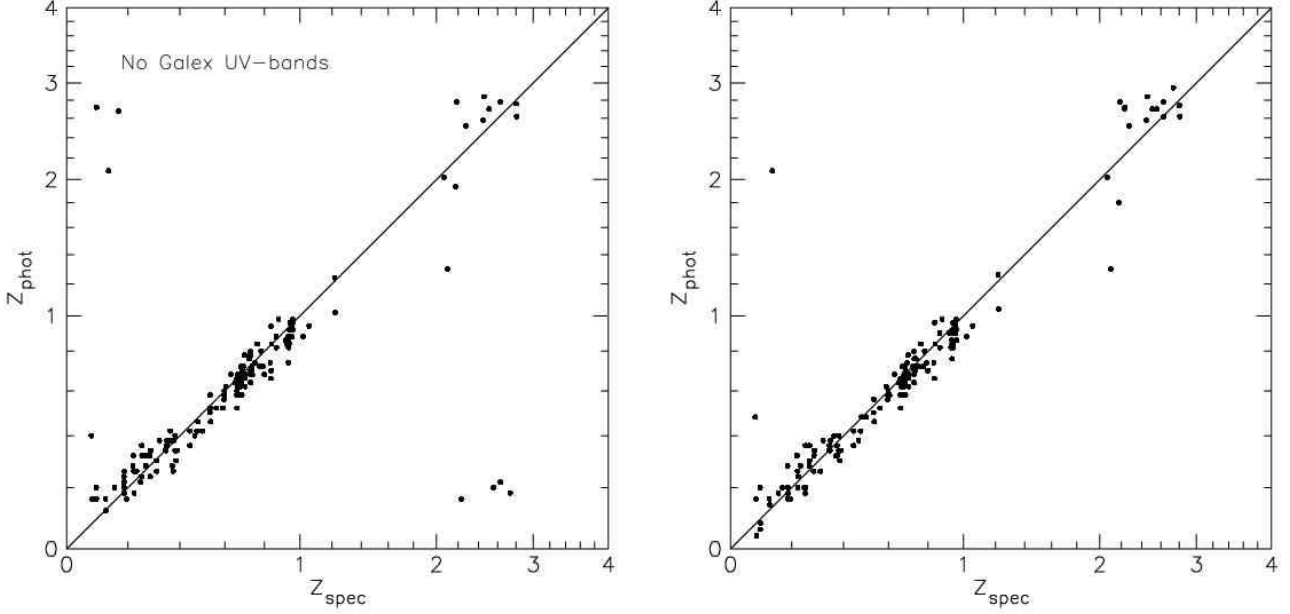


Figure 10. Comparison of spectroscopic and photometric redshifts in the COSMOS field (162 galaxies). Left panel: u band to K band are used to derive the photometric redshifts. Right panel: u band to K band as well as the GALEX FUV and NUV bands are used to derive the photometric redshifts.

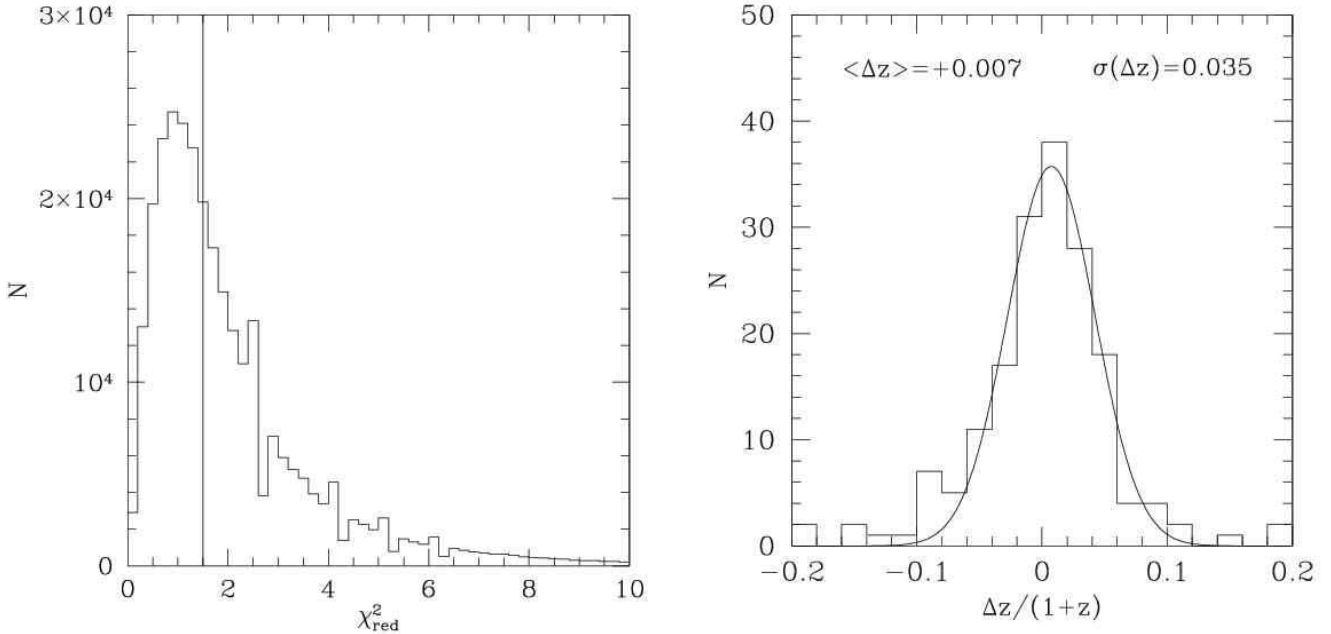


Figure 11. Left panel: Histogram of the reduced χ^2 for all galaxies in the COSMOS field as obtained for the best fitting template and redshift. The dotted vertical line indicates the median reduced χ^2 of 1.5. Right panel: Histogram of the photometric redshift errors. The error distribution can be approximated by a Gaussian centred at 0.007 with an rms of 0.035 (solid line).

$$p_z(z) = \text{Const} \times \frac{\beta z^2}{\Gamma(3/\beta) z_0^3} \exp\left(-(z/z_0)^\beta\right) \quad (7)$$

where Const , $z_0 = \langle z \rangle \frac{\Gamma(3/\beta)}{\Gamma(4/\beta)}$ and β are free parameters with $\langle z \rangle$ being the first moment of the distribution and Γ the Gamma function. The best fitting values are: $\text{Const} = 6206$, $z_0 = 0.107$, and $\beta = 0.611$.

Please note that if we analyse the galaxy photometric redshift histogram with a binning of $\Delta z = 0.1$ there are three clearly visible peaks below redshift of $z = 2$: one at $z_{\text{phot}} = [0.6, 0.7]$, one at $z_{\text{phot}} = [0.9, 1.0]$, and one at $z_{\text{phot}} = [1.7, 1.8]$. Interestingly, we also find peaks in the spectroscopic redshift histogram (see also Fig. 9) with at least 10

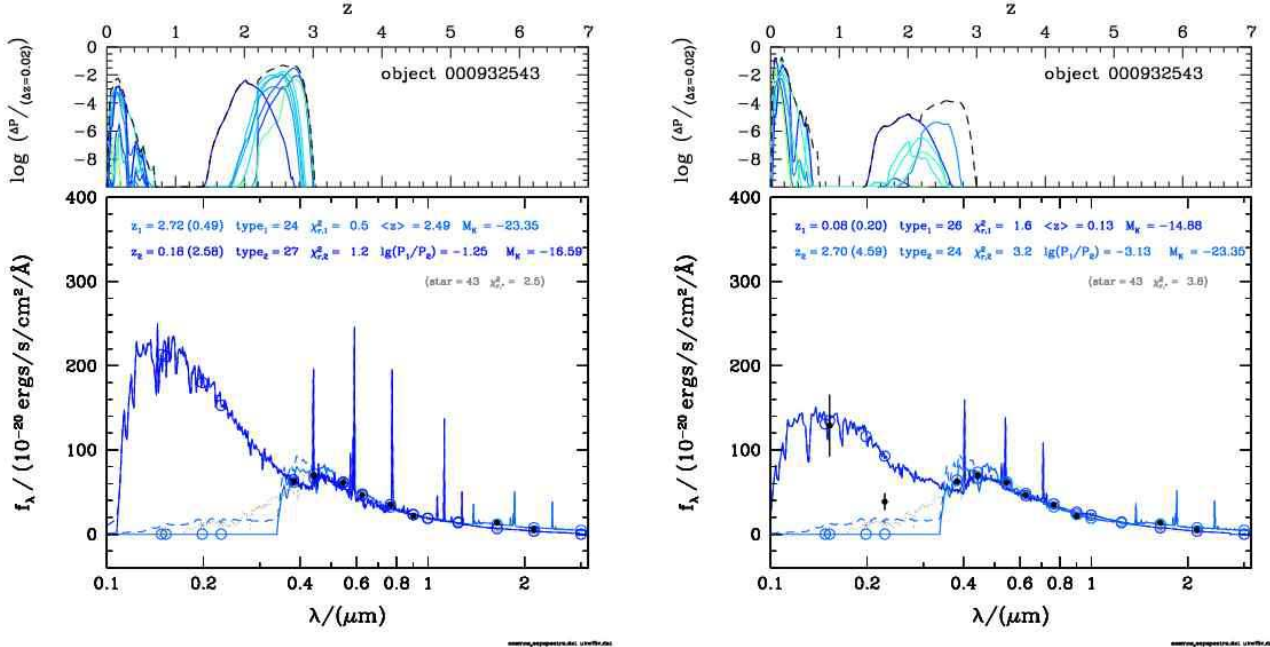


Figure 12. Redshift probability distribution (upper part) and photometric redshift fit (lower part) of the spectroscopic object 000932543 with $z_{\text{spec}} = 0.093$. The different SEDs are colour coded. The open circles (lower part) represent the SED integrated within the various filter transmission curves, whereas the black dots represent the measured fluxes. The redshift for the best fitting SED (z_1) as well as for the second best fit (z_2) are also given. Left panel: Only 8 bands (u-band to K-band) are used to derive the photometric redshift yielding a wrong z_{phot} of 2.72. Right panel: 10 bands (FUV, NUV, u-band to K-band) are used to derive the photometric redshift yielding a z_{phot} of 0.08 very close to the spectroscopic redshift.

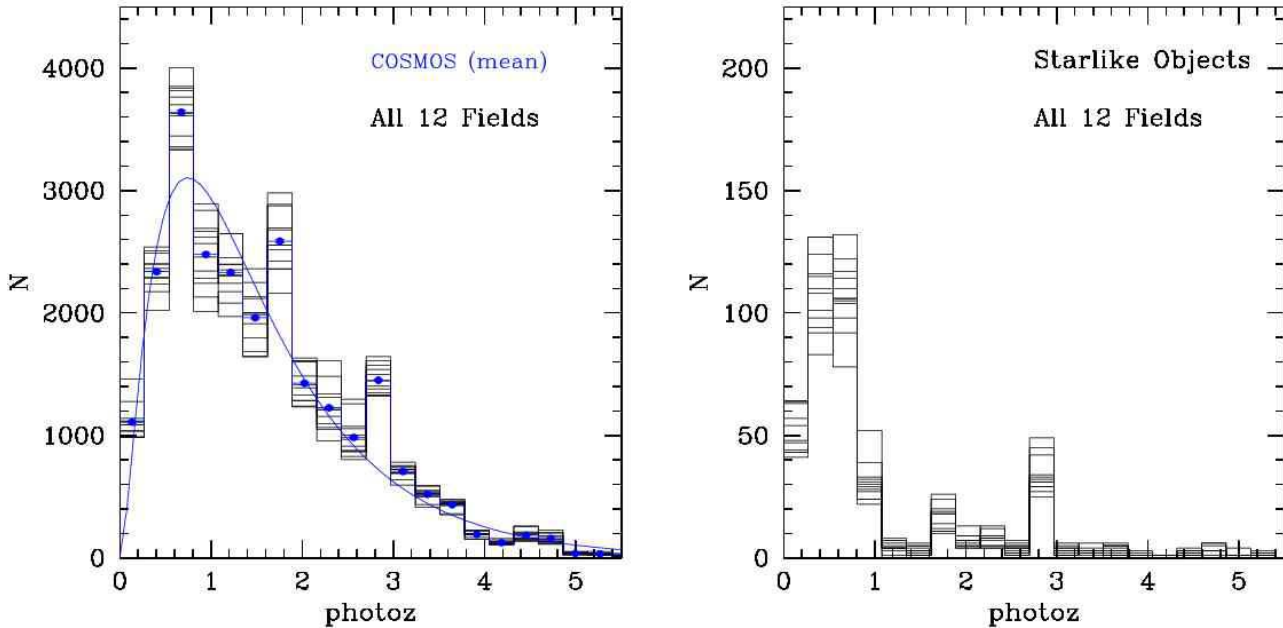


Figure 13. Left panel: Redshift number distribution of all galaxies in the 12 patches. The mean number distribution is shown as blue dots. The blue solid line represents a fit to the mean galaxy distribution using the approach of Brainerd et al. (1996) (see text for details). Right panel: Redshift distribution of objects classified as stars (see text for details) and eliminated from the final galaxy catalogues. Please note the different scaling by a factor of 20 in the left and right panel.

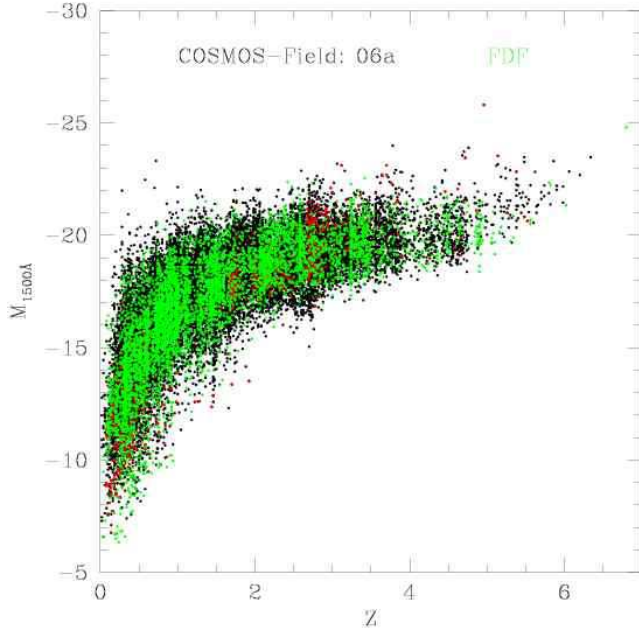


Figure 14. Absolute UV-band magnitudes of galaxies in the COSMOS 06a patch (black dots) as a function of redshift. The green dots are derived in the FDF whereas the red dots represent COSMOS objects classified as stars if a more conservative criterion in separating stars from galaxies ($\chi^2_{star} < \chi^2_{galaxy} \Rightarrow star$; see text for details) is applied.

galaxies at $z_{spec} = [0.657, 0.669]$, $z_{spec} = [0.672, 0.683]$, and $z_{spec} = [0.926, 0.941]$.

7 UV LUMINOSITY FUNCTION AND DENSITY

In this section we show the UV luminosity function (LF) at 1500 Å as derived from our deep *i*-selected catalogue and compare it to the LFs in the FDF (Gabasch et al. 2004a). Note that in this paper we are not aiming to give a complete analysis of the LF evolution. A detailed analysis of the LFs derived in different passbands as well as the star-formation rate (SFR) together with an elaborate comparison to the recent literature will be presented in future papers. Here we limit ourselves to a one-to-one comparison with the FDF luminosity functions (mostly as a consistency check to our earlier work).

To derive the absolute UV band magnitude we use the best fitting SED as determined by the photometric redshift code. Since the photometric redshift code works with aperture fluxes, we only need to correct to total luminosities by applying an object dependent scale factor. For this scale factor we used the ratio of the I-band aperture flux to the total flux as provided by SExtractor (MAG_APER and MAG_AUTO). As the SED fits all observed-frame passbands simultaneously, possible systematic errors which could be introduced by using K-corrections applied to a single observed magnitude are reduced (see Gabasch et al. 2004a, for more details).

As an example, we plot in Fig. 14 the absolute UV-band

magnitudes against the photometric redshifts of the objects in the COSMOS patch 06a. Moreover we also show the absolute UV-band magnitudes as derived in the FDF. Both fields agree very well in their magnitude distribution, although there are a few relatively bright objects in the COSMOS patch (about 5 times the area of the FDF) not seen in the FDF distribution. To check if those objects could be stars misclassified as galaxies by our star-galaxy separation criterion, we decided to use a more conservative criterion for separating stars from galaxies. We changed our criterion from $2 \chi^2_{star} < \chi^2_{galaxy}$ to $\chi^2_{star} < \chi^2_{galaxy}$ (see above). As can be seen in Fig. 14 even this conservative criterion does not remove a substantial fraction of these relatively bright objects. Note that because of the larger seeing (0.95'' compared to the FDF (0.55''), there may be more blended objects in the catalogue.

The luminosity function is computed by dividing the number of galaxies in each magnitude bin by the volume V_{bin} of the redshift interval. To account for the fact that some fainter galaxies are not visible in the whole survey volume, we performed a V/V_{max} (Schmidt 1968) correction. The errors of the LFs were calculated by means of Monte-Carlo simulations and include the photometric redshift error of every single galaxy, as well as the statistical error (Poissonian error). To derive precise Schechter parameters, we limited our analysis of the LF to the magnitude bin where the V/V_{max} correction is negligible (red dots in Fig. 15). We also show the uncorrected LF in the various plots as open circles. We did not assume any evolution of the galaxies within the single redshift bins. The redshift intervals are approximately the same size in $\ln(1+z)$, and most of the results we are going to discuss are based on 1000 – 4000 galaxies per redshift bin and per patch.

In Fig. 15 we present the UV luminosity functions at 1500 Å (we evaluate the luminosity function in the rectangular filter at 1500 ± 100 Å). The filled (open) symbols denote the luminosity function with (without) completeness correction in the different patches. We also show the V/V_{max} corrected mean LFs in the COSMOS field as well as the FDF LFs (Gabasch et al. 2004a). The solid red lines show the Schechter function fitted to the luminosity function (we used a fixed slope of $\alpha = -1.07$ as found in the FDF). The best fitting Schechter parameter, the redshift binning as well as the reduced χ^2 are also listed.

It is obvious from the figure that there is strong evolution in characteristic luminosity and number density between redshifts 0.6 and 4.5. This can be best seen in Fig. 16, where we show the redshift evolution of M^* and ϕ^* as derived from the Schechter functions fitted to the LFs of Fig. 15. Please note that we used only magnitude bins with a V/V_{max} correction of about unity. Moreover we exclude also very bright magnitude bins as there might be a contamination by spurious detections, stars, AGNs or blended objects. The magnitude bins used for deriving the best fitting Schechter parameters are shown in Fig. 15 as red dots. Nevertheless, including also the very bright bins changes the best fitting values only negligibly. We find a substantial brightening of M^* and a decrease of ϕ^* with redshift: from $\langle z \rangle \sim 0.5$ to $\langle z \rangle \sim 4.5$ the characteristic magnitude increases by about 3 magnitudes, whereas the characteristic density decreases by about 80 – 90%. Note that our results do not disagree with recent findings of e.g. Bouwens et al. (2006, 2007) who are

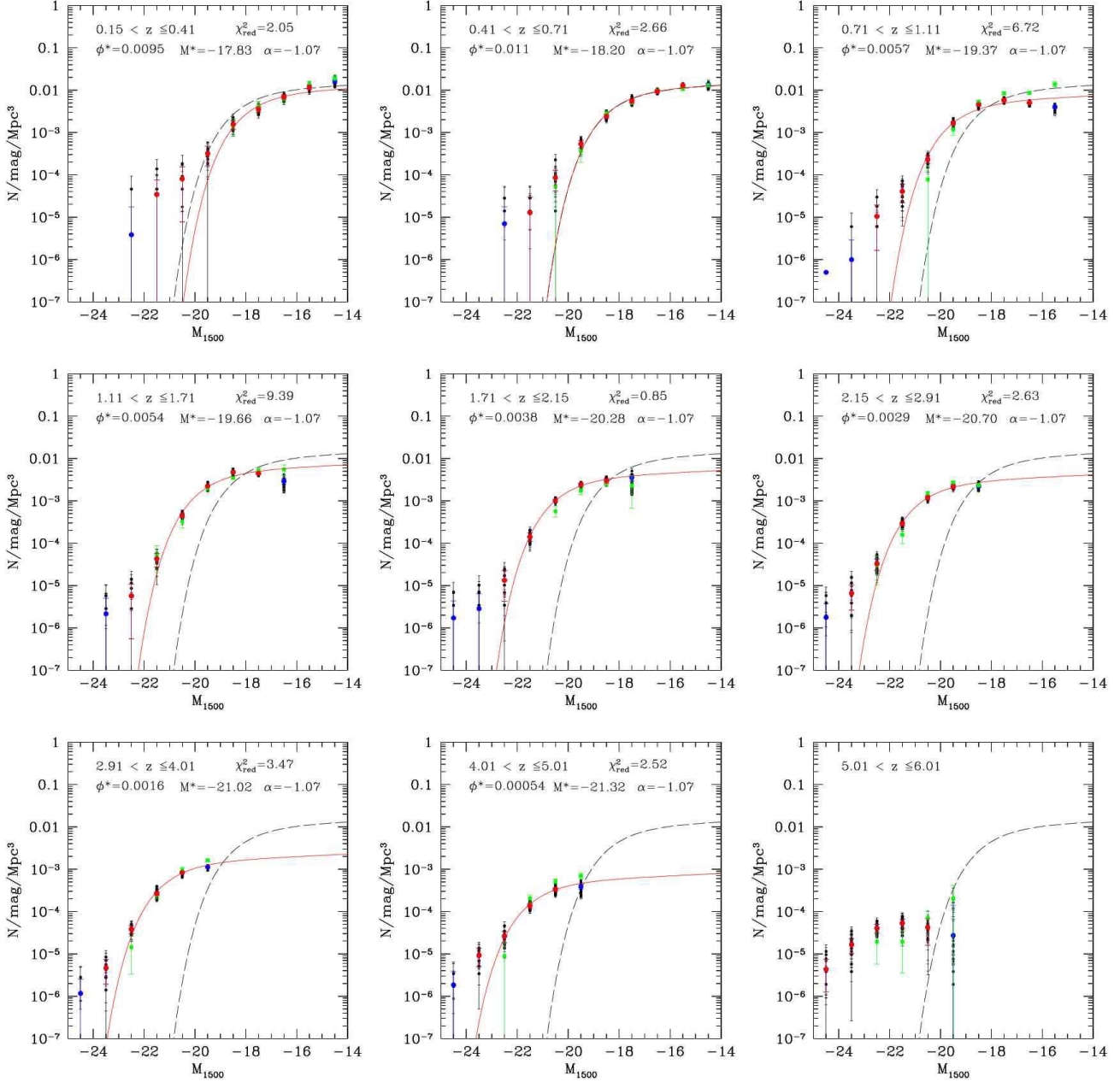


Figure 15. Luminosity functions at 1500 \AA from low redshift ($\langle z \rangle = 0.3$, upper left panel) to high redshift ($\langle z \rangle = 5.5$, lower right panel). The filled (open) black symbols show the luminosity function corrected (uncorrected) for V/V_{max} in the various patches. The red and the blue dots represent the mean LF in the field. The green squares represent the LFs as derived in the FDF. The fitted Schechter functions for a fixed slope α are shown as solid red lines (only the red dots are used to derive the best fitting Schechter functions). Note that we only fit the luminosity functions to $\langle z \rangle = 4.5$. The parameters of the Schechter functions can be found in Table 5. The Schechter fit for redshift $\langle z \rangle = 0.6$ is indicated as a dashed black line in all panels.

tracing the UV LF from $z \sim 3$ to $z \sim 6$ and find a faintening of M^* (with increasing redshift) and nearly no density evolution in this redshift range since we limit our analysis to redshifts of $z \lesssim 4.5$. As discussed in Bouwens et al. (2007) it is plausible that there is a turnover in the LF evolution at redshift of $z \sim 4$.

The best fitting Schechter parameters and their 1σ errors in the COSMOS field are summarised in Table 5. In Fig. 16 we also show the redshift evolution of M^* and ϕ^* as derived in

the FDF by Gabasch et al. (2004a). Although in the COSMOS field the characteristic magnitude is about 0.25 mag brighter in most of the redshift bins if compared to the FDF results, the characteristic density is slightly lower. This results in a very similar UV luminosity density (LD; the integrated light emitted by the galaxies) in the COSMOS field and in the FDF, as can be seen in Fig. 17.

The LD at a given redshift is derived by summing the completeness-corrected (using a V/V_{max} correction) lumi-

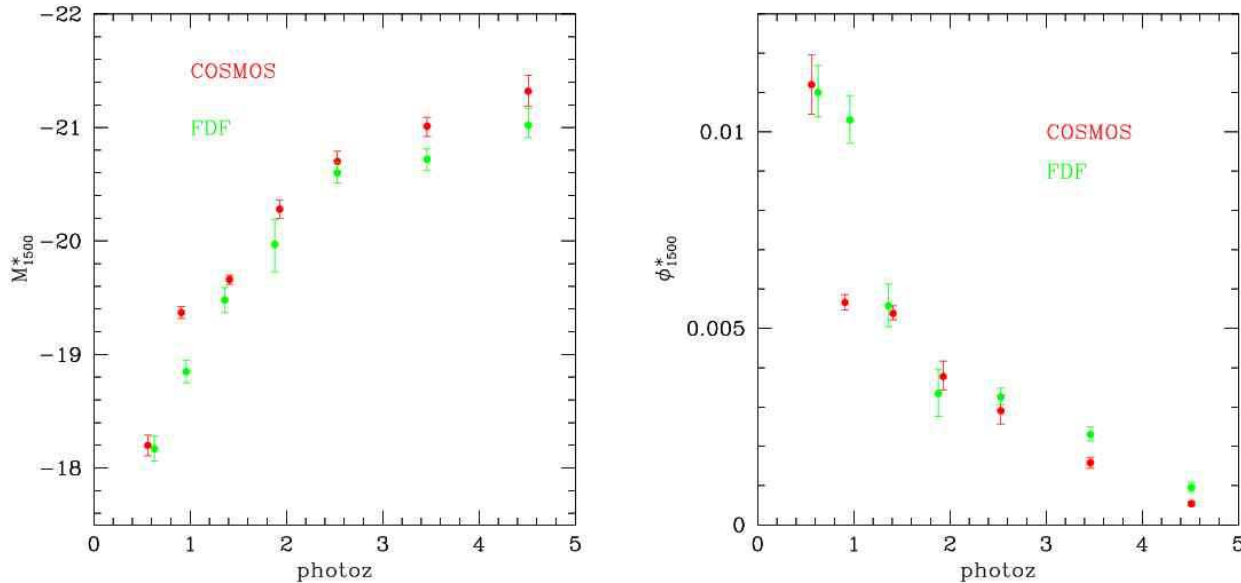


Figure 16. Redshift evolution of M^* (left panel) and ϕ^* (right panel) for the UV band at 1500 Å. The red dots are derived from the mean luminosity function in the COSMOS field (Schechter fit to the red dots in Fig. 15) whereas the green dots stem from the FDF.

Table 5. Schechter function fit at 1500 Å

redshift interval	M^* (mag)	ϕ^* (Mpc^{-3})	α (fixed)
0.41 – 0.71	$-18.20 \pm 0.09 - 0.09$	$1.12\text{e-}02 \pm 7.61\text{e-}04 - 7.61\text{e-}04$	-1.07
0.71 – 1.11	$-19.37 \pm 0.05 - 0.05$	$5.66\text{e-}03 \pm 1.97\text{e-}04 - 1.97\text{e-}04$	-1.07
1.11 – 1.71	$-19.66 \pm 0.04 - 0.04$	$5.38\text{e-}03 \pm 1.97\text{e-}04 - 1.69\text{e-}04$	-1.07
1.71 – 2.15	$-20.28 \pm 0.08 - 0.08$	$3.77\text{e-}03 \pm 3.94\text{e-}04 - 3.38\text{e-}04$	-1.07
2.15 – 2.91	$-20.70 \pm 0.09 - 0.09$	$2.90\text{e-}03 \pm 3.94\text{e-}04 - 3.38\text{e-}04$	-1.07
2.91 – 4.01	$-21.01 \pm 0.08 - 0.09$	$1.58\text{e-}03 \pm 1.41\text{e-}04 - 1.41\text{e-}04$	-1.07
4.01 – 5.01	$-21.32 \pm 0.14 - 0.13$	$5.35\text{e-}04 \pm 5.63\text{e-}05 - 5.63\text{e-}05$	-1.07

osity of every single galaxy up to the absolute magnitude limit. Contrary to the procedure described in Gabasch et al. (2004b) and Gabasch et al. (2006), we do *not* apply a further correction (to zero galaxy luminosity), to take the missing contribution to the LD of the fainter galaxies into account. This further correction should be done only after a very careful analysis of the LFs (as it requires an extrapolation of the LF at the faint end) and is postponed to a future paper. As the limiting *i*-band magnitudes of the COSMOS field and the FDF are very similar, we decided to integrate the LF in both fields down to the same absolute magnitude instead (see Table 6). This approach allows us to directly compare the LD of both fields without relying on any extrapolation.

In Fig. 17 we show the 1500Å luminosity densities of the single COSMOS patches, the mean COSMOS LD as well as the LD derived in the FDF. The FDF and COSMOS luminosity densities are integrated down to the faint-end limiting magnitudes given in Table 6. Moreover we also show the COSMOS luminosity densities integrated between the faint-end and a bright-end limiting magnitude (see Table 6). The bright-end cut excludes in total 80 (0.03%) bright objects in the COSMOS field. It was derived by comparing the Schechter-fit to the LF (the excluded LF bins are shown as

blue dots at the bright end in Fig 15) as well as by comparing the absolute UV-band magnitudes as a function of redshift with those in the FDF (see Fig. 14 for one patch). Fig. 17 nicely shows that the UV LD and its redshift evolution in the FDF (based on a very small field if compared to the COSMOS field) agrees quite well with the result in the COSMOS field. Even though for redshifts below $z \sim 2.5$ the UV LD in the FDF is systematically lower than the value in the COSMOS field the deviation is in the order of 1σ . The values of the mean COSMOS LD together with the error bars are listed in Table 6.

8 SUMMARY AND CONCLUSIONS

In this paper we present the data acquisition and reduction of NIR Js, H, and K' bands in the COSMOS field. We describe a 2-pass reduction pipeline to reduce NIR data. The 2-pass pipeline is optimised to avoid flat-field errors introduced if the latter are constructed from science exposures. Moreover we present and implement a method to stack images of different quality resulting in an optimal S/N ratio for faint sky dominated point sources. The Js and K' band cover an area of about 200arcmin^2 (1 patch) whereas the H band

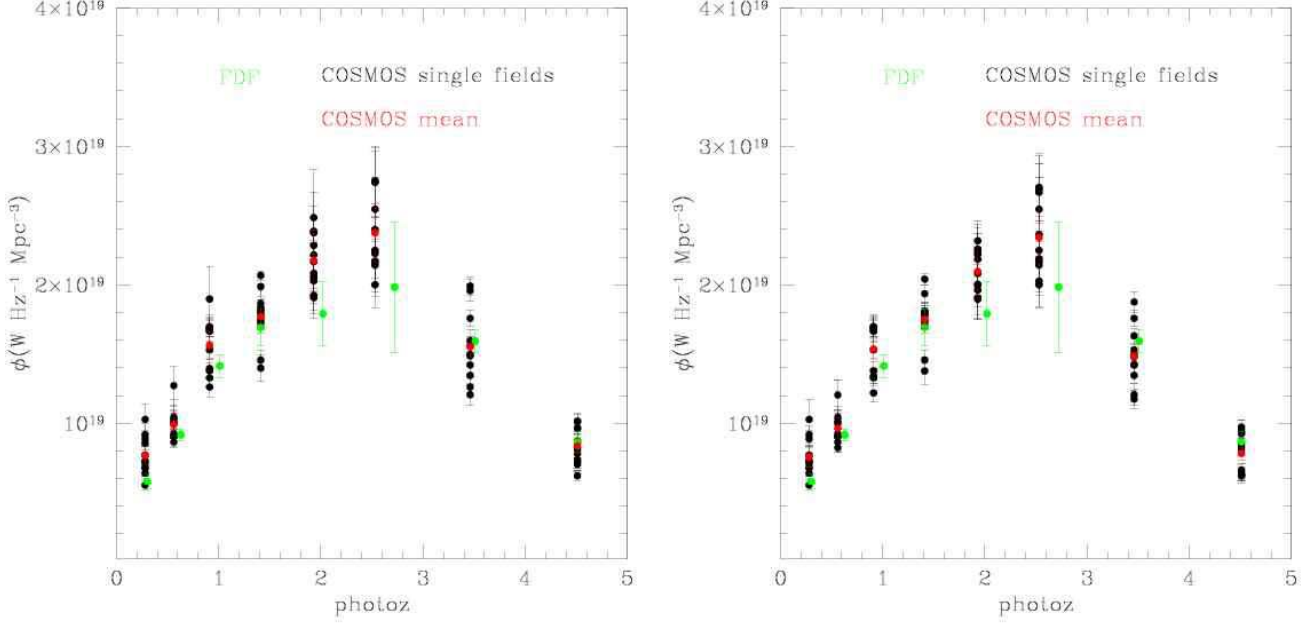


Figure 17. The 1500 Å luminosity densities of the single COSMOS patches (black dots), the mean COSMOS LD (red dots) as well as the LD derived in the FDF (green dots). Left panel: The luminosity densities are integrated between the faint-end limiting magnitudes given in Table 6 but *no* limiting magnitude cut was used for the bright-end. Right panel: The luminosity densities are integrated between the faint-end and the bright-end limiting magnitudes given in Table 6. The values of the mean COSMOS LD together with the error bars are listed in Table 6.

Table 6. The mean COSMOS LD at 1500 Å for the different redshift bins. The luminosity densities are derived within the faint-end and the bright-end limiting magnitudes given in the last column.

redshift	luminosity density (W Hz ⁻¹ Mpc ⁻³)	magnitude range
0.15 – 0.41	7.557e+18 ± 7.243e+17	-14. – -22.
0.41 – 0.71	9.640e+18 ± 7.219e+17	-14. – -22.
0.71 – 1.11	1.536e+19 ± 7.329e+17	-15. – -23.
1.11 – 1.71	1.750e+19 ± 6.290e+17	-16. – -23.
1.71 – 2.15	2.097e+19 ± 1.719e+18	-17. – -23.
2.15 – 2.91	2.340e+19 ± 2.116e+18	-18. – -24.
2.91 – 4.01	1.485e+19 ± 6.931e+17	-19. – -24.
4.01 – 5.01	7.809e+18 ± 4.728e+17	-19. – -24.
5.01 – 6.01	6.052e+18 ± 8.592e+17	-19. – -25.

covers about 0.85° (15 patches) in total. The 50% completeness limits are 22.67, ~ 21.9 , and 21.76 in the Js, H, and K' band, respectively. The number counts of all NIR bands nicely agree with the number counts taken from literature.

Furthermore we present a deep and homogeneous i-band selected multi-waveband catalogue in the COSMOS field by combining publicly available u, B, V, r, i, z, and K bands with the H band. The clean catalogue with a formal 50% completeness limit for point sources of $i \sim 26.7$ comprises about 290 000 galaxies with information in 8 passbands and covers an area of about 0.7° (12 patches). We exclude all objects with corrupted magnitudes in only one of the filters from the catalogue in order to have a catalogue as homogeneous as possible.

Photometric redshifts for all objects are derived and a comparison with 162 spectroscopic redshifts in the redshift range $0 \lesssim z \lesssim 3$ shows that the achieved accuracy of the photometric redshifts is $\Delta z / (z_{\text{spec}} + 1) \lesssim 0.035$ with only $\sim 2\%$ outliers. Please note that in order to break the degeneracy between high redshift and low redshift solutions we included also the GALEX FUV and NUV filters in the photometric redshift estimation which considerably reduced the number of outliers.

The multi-waveband catalogue including the photometric redshift information is made publicly available. The data can be downloaded from `\protect\vrulewidth0pthttp://www.mpe.mpg.de/~gabasch/COSMOS/`

We derive absolute UV magnitudes and a comparison in a magnitude-redshift diagram with the FDF shows good agreement. Moreover we investigate the evolution of the luminosity function evaluated in the restframe UV (1500 Å). We find a substantial brightening of M^* and a decrease of ϕ^* with redshift: from $\langle z \rangle \sim 0.5$ to $\langle z \rangle \sim 4.5$ the characteristic magnitude increases by about 3 magnitudes, whereas the characteristic density decreases by about 80 – 90%.

We compare the redshift evolution of the UV luminosity density in the COSMOS field and the FDF up to a redshift of $z \sim 5$. Below a redshift of $z \sim 2.5$ the mean UV luminosity density in COSMOS is systematically higher by about 1σ if compared to the FDF. At $2.5 \lesssim z \lesssim 5$ both UV luminosity densities agree very well.

It is worth noting the remarkably good agreement between the UV LF as well as the UV LD despite the fact, that the FDF is about 60 times smaller than the COSMOS field analysed here.

ACKNOWLEDGEMENTS

We thank the anonymous referee for his helpful comments which improved the presentation of the paper. The authors would like to thank the staff at Calar Alto Observatory for their support during the observations which were taken in a collaborative effort with the HIROCS team of Dr. H.-J. Röser (MPIA Heidelberg) and the ALHAMBRA team of Dr. M. Moles (IAA Granada). We thank both teams for the kind collaboration during the preparation and execution of the program and Dr. Röser and team for useful discussions during data reduction. AG thanks G. Feulner, J. Fliri, and A. Halkola for a careful and critical reading of the manuscript and for their valuable suggestions. The authors thank Ralf Bender for providing the photometric redshift code. The authors also thanks Nigel Metcalfe for making number count data available in electronic form. This work was supported by the *Deutsche Forschungsgemeinschaft*, DFG, SFB 375 (Astroteilchenphysik).

REFERENCES

- Arnouts, S., D’Odorico, S., Cristiani, S., et al. 1999a, *A&A*, 341, 641
 —. 1999b, *A&A*, 341, 641
 Arnouts, S., Vandame, B., Benoist, C., et al. 2001a, *A&A*, 379, 740
 —. 2001b, *A&A*, 379, 740
 Baum, W. A. 1962, in *IAU Symp. 15: Problems of Extra-Galactic Research*, Vol. 15, 390
 Bender, R. et al. 2001, in *ESO/ECF/STScI Workshop on Deep Fields*, ed. S. Cristiani (Berlin: Springer), 96
 Benítez, N. 2000, *ApJ*, 536, 571
 Bershad, M. A., Lowenthal, J. D., & Koo, D. C. 1998, *ApJ*, 505, 50
 Bertin, E. 2006, in *ASP Conf. Ser. 351: Astronomical Data Analysis Software and Systems XV*, ed. C. Gabriel, C. Arviset, D. Ponz, & S. Enrique, 112
 Bertin, E. & Arnouts, S. 1996, *A&AS*, 117, 393
 Bertin, E. 2003, *Swarp user’s guide*
 Bouwens, R. J., Illingworth, G. D., Blakeslee, J. P., & Franx, M. 2006, *ApJ*, 653, 53
 Bouwens, R. J., Illingworth, G. D., Franx, M., & Ford, H. 2007, *UV Luminosity Functions at z4, 5, and 6 from the HUDF and other Deep HST ACS Fields: Evolution and Star Formation History*
 Bouwens, R. J., Illingworth, G. D., Thompson, R. I., et al. 2004, *ApJ*, 606, L25
 Brainerd, T. G., Blandford, R. D., & Smail, I. 1996, *ApJ*, 466, 623
 Brunner, R. J., Connolly, A. J., & Szalay, A. S. 1999, *ApJ*, 516, 563
 Bunker, A. J., Stanway, E. R., Ellis, R. S., & McMahon, R. G. 2004, *MNRAS*, 450
 Capak, P., Cowie, L. L., Hu, E. M., et al. 2004, *AJ*, 127, 180
 Casertano, S., de Mello, D., Dickinson, M., et al. 2000, *AJ*, 120, 2747
 Casertano, S., Ratnatunga, K. U., Griffiths, R. E., et al. 1995, *ApJ*, 453, 599
 Chen, H.-W., McCarthy, P. J., Marzke, R. O., et al. 2002, *ApJ*, 570, 54
 Cimatti, A., Mignoli, M., Daddi, E., et al. 2002, *A&A*, 392, 395
 Colless, M., Dalton, G., Maddox, S., et al. 2001, *MNRAS*, 328, 1039
 Cristóbal-Hornillos, D., Balcells, M., Prieto, M., et al. 2003, *ApJ*, 595, 71
 Daddi, E., Cimatti, A., Renzini, A., et al. 2004, *ApJ*, 617, 746
 Djorgovski, S., Soifer, B. T., Pahre, M. A., et al. 1995, *ApJ*, 438, L13
 Driver, S. P., Windhorst, R. A., Ostrander, E. J., et al. 1995, *ApJ*, 449, L23
 Drory, N., Feulner, G., Bender, R., et al. 2001a, *MNRAS*, 325, 550
 —. 2001b, *MNRAS*, 325, 550
 Ellis, R. S., Colless, M., Broadhurst, T., Heyl, J., & Glazebrook, K. 1996, *MNRAS*, 280, 235
 Ferguson, H. C., Dickinson, M., & Williams, R. 2000, *ARA&A*, 38, 667
 Fernández-Soto, A., Lanzetta, K. M., & Yahil, A. 1999, *ApJ*, 513, 34
 Feulner, G., Bender, R., Drory, N., et al. 2003, *MNRAS*, 342, 605
 Firth, W. J., Metcalfe, N., & Shanks, T. 2006, *MNRAS*, 371, 1601
 Gabasch, A., Bender, R., Seitz, S., et al. 2004a, *A&A*, 421, 41
 Gabasch, A., Hopp, U., Feulner, G., et al. 2006, *A&A*, 448, 101
 Gabasch, A., Salvato, M., Saglia, R. P., et al. 2004b, *ApJ*, 616, L83
 Gardner, J. P., Cowie, L. L., & Wainscoat, R. J. 1993, *ApJ*, 415, L9
 Gardner, J. P., Sharples, R. M., Carrasco, B. E., & Frenk, C. S. 1996, *MNRAS*, 282, L1
 Gawiser, E., van Dokkum, P. G., Herrera, D., et al. 2006, *ApJS*, 162, 1
 Gialalisco, M. 2002, *ARA&A*, 40, 579
 Gialalisco, M., Dickinson, M., Ferguson, H. C., et al. 2004a, *ApJ*, 600, L103
 Gialalisco, M., Ferguson, H. C., Koekemoer, A. M., et al. 2004b, *ApJ*, 600, L93
 Glazebrook, K., Peacock, J. A., Miller, L., & Collins, C. A. 1995, *MNRAS*, 275, 169
 Grazian, A., Fontana, A., de Santis, C., et al. 2006, *A&A*, 449, 951
 Hall, P. & Mackay, C. D. 1984, *MNRAS*, 210, 979
 Heidt, J., Appenzeller, I., Gabasch, A., et al. 2003, *A&A*, 398, 49
 Horne, K. 1986, *PASP*, 98, 609
 Huang, J., Cowie, L. L., & Luppino, G. A. 1998, *ApJ*, 496, 31
 Huang, J. S., Cowie, L. L., Gardner, J. P., et al. 1997, *ApJ*, 476, 12
 Huang, J.-S., Thompson, D., Kümmel, M. W., et al. 2001, *A&A*, 368, 787
 Jarrett, T. H., Chester, T., Cutri, R., et al. 2000, *AJ*, 119, 2498
 Kümmel, M. W. & Wagner, S. J. 2001, *A&A*, 370, 384
 Koo, D. C. 1985, *AJ*, 90, 418
 Labbé, I., Franx, M., Rudnick, G., et al. 2003, *AJ*, 125, 1107

- Le Borgne, D. & Rocca-Volmerange, B. 2002, *A&A*, 386, 446
- Le Fèvre, O., Mellier, Y., McCracken, H. J., et al. 2004, *A&A*, 417, 839
- Le Fèvre, O., Saisse, M., Mancini, D., et al. 2003, in *Instrument Design and Performance for Optical/Infrared Ground-based Telescopes*. Edited by Iye, Masanori; Moorwood, Alan F. M. *Proceedings of the SPIE*, Volume 4841, pp. 1670-1681 (2003)., ed. M. Iye & A. F. M. Moorwood, 1670-1681
- Lilly, S. J., Cowie, L. L., & Gardner, J. P. 1991, *ApJ*, 369, 79
- Lilly, S. J., Fèvre, O. L., Renzini, A., et al. 2007, *ApJS*, 172, 70
- Lilly, S. J., Le Fèvre, O., Crampton, D., Hammer, F., & Tresse, L. 1995, *ApJ*, 455, 50
- Maihara, T., Iwamuro, F., Tanabe, H., et al. 2001a, *PASJ*, 53, 25
- . 2001b, *PASJ*, 53, 25
- Martini, P. 2001a, *AJ*, 121, 598
- . 2001b, *AJ*, 121, 598
- McCracken, H. J., Metcalfe, N., Shanks, T., et al. 2000a, *MNRAS*, 311, 707
- . 2000b, *MNRAS*, 311, 707
- McLeod, B. A., Bernstein, G. M., Rieke, M. J., Tollestrup, E. V., & Fazio, G. G. 1995, *ApJS*, 96, 117
- Metcalfe, N., Shanks, T., Campos, A., McCracken, H. J., & Fong, R. 2001a, *MNRAS*, 323, 795
- . 2001b, *MNRAS*, 323, 795
- Metcalfe, N., Shanks, T., Weilbacher, P. M., et al. 2006, *MNRAS*, 370, 1257
- Minowa, Y. et al. 2005, *ApJ*, in press, astro-ph/0505348
- Moles, M., Alfaro, E., Benitez, N., et al. 2005, astro-ph/0504545
- Moustakas, L. A., Davis, M., Graham, J. R., et al. 1997, *ApJ*, 475, 445
- Moy, E., Barmby, P., Rigopoulou, D., et al. 2003, *A&A*, 403, 493
- Noll, S., Mehlert, D., Appenzeller, I., et al. 2004, *A&A*, 418, 885
- Ouchi, M., Shimasaku, K., Furusawa, H., et al. 2003, *ApJ*, 582, 60
- Pickles, A. J. 1998, *PASP*, 110, 863
- Postman, M., Lauer, T. R., Szapudi, I., & Oegerle, W. 1998, *ApJ*, 506, 33
- Quadri, R., Marchesini, D., van Dokkum, P., et al. 2007, *AJ*, 134, 1103
- Rix, H.-W., Barden, M., Beckwith, S. V. W., et al. 2004, *ApJS*, 152, 163
- Röser, H.-J., Hippelein, H. H., & Wolf, C. 2004, in *Clusters of Galaxies: Probes of Cosmological Structure and Galaxy Evolution*, ed. J. S. Mulchaey, A. Dressler, & A. Oemler
- Saracco, P., D'Odorico, S., Moorwood, A., et al. 1999, *A&A*, 349, 751
- Saracco, P., Giallongo, E., Cristiani, S., et al. 2001, *A&A*, 375, 1
- Saracco, P., Iovino, A., Garilli, B., Maccagni, D., & Chincarini, G. 1997, *AJ*, 114, 887
- Sawicki, M. & Thompson, D. 2005, *ApJ*, 635, 100
- Schmidt, M. 1968, *ApJ*, 151, 393
- Scodeggio, M., Franzetti, P., Garilli, B., et al. 2005, *PASP*, 117, 1284
- Scoville, N., Aussel, H., Brusa, M., et al. 2007, *ApJS*, 172, 1
- Snigula, J., Drory, N., Bender, R., et al. 2002, *MNRAS*, 336, 1329
- Soifer, B. T., Matthews, K., Djorgovski, S., et al. 1994, *ApJ*, 420, L1
- Stanford, S. A., Eisenhardt, P. R. M., & Dickinson, M. 1995, *ApJ*, 450, 512
- Steidel, C. C., Giavalisco, M., Dickinson, M., & Adelberger, K. L. 1996, *AJ*, 112, 352
- Steidel, C. C. & Hamilton, D. 1993, *AJ*, 105, 2017
- Steidel, C. C., Shapley, A. E., Pettini, M., et al. 2004, *ApJ*, 604, 534
- Stoughton, C., Lupton, R. H., Bernardi, M., et al. 2002, *AJ*, 123, 485
- Szokoly, G. P., Subbarao, M. U., Connolly, A. J., & Mobasher, B. 1998, *ApJ*, 492, 452
- Teplitz, H. I., Gardner, J. P., Malumuth, E. M., & Heap, S. R. 1998, *ApJ*, 507, L17
- Teplitz, H. I., McLean, I. S., & Malkan, M. A. 1999, *ApJ*, 520, 469
- Thompson, R. I., Storrie-Lombardi, L. J., Weymann, R. J., et al. 1999, *AJ*, 117, 17
- Tyson, J. A. 1988, *AJ*, 96, 1
- Väisänen, P., Tollestrup, E. V., Willner, S. P., & Cohen, M. 2000, *ApJ*, 540, 593
- Williams, R. E., Baum, S., Bergeron, L. E., et al. 2000, *AJ*, 120, 2735
- Williams, R. E., Blacker, B., Dickinson, M., et al. 1996a, *AJ*, 112, 1335
- . 1996b, *AJ*, 112, 1335
- Wolf, C., Meisenheimer, K., Rix, H.-W., et al. 2003, *A&A*, 401, 73
- Yan, L., McCarthy, P. J., Storrie-Lombardi, L. J., & Weymann, R. J. 1998, *ApJ*, 503, L19
- Yasuda, N. et al. 2001, *AJ*, 122, 1104
- Yee, H. K. C., Ellingson, E., & Carlberg, R. G. 1996, *ApJS*, 102, 269
- Zatloukal, M., Roser, H. J., Wolf, C., Hippelein, H., & Falter, S. 2007, Distant galaxy clusters in the COSMOS field found by HIROCS